Redox Biology 39 (2021) 101838

Contents lists available at ScienceDirect

Redox Biology

journal homepage: www.elsevier.com/locate/redox

Research Paper

Genomic *GLO1* deletion modulates *TXNIP* expression, glucose metabolism, and redox homeostasis while accelerating human A375 malignant melanoma tumor growth

Jana Jandova, Georg T. Wondrak *

Department of Pharmacology and Toxicology, College of Pharmacy and UA Cancer Center, University of Arizona, Tucson, AZ, USA

ARTICLE INFO

Keywords:
NanoString nCounter™ expression profiling
Malignant melanoma
Glyoxalase 1
Thioredoxin-interacting protein
Glucose transporter 1
Tumorigenesis

ABSTRACT

Glyoxalase 1 (encoded by *GLO1*) is a glutathione-dependent enzyme detoxifying the glycolytic byproduct methylglyoxal (MG), an oncometabolite involved in metabolic reprogramming. Recently, we have demonstrated that *GLO1* is overexpressed in human malignant melanoma cells and patient tumors and substantiated a novel role of *GLO1* as a molecular determinant of invasion and metastasis in melanoma. Here, employing NanoString™ gene expression profiling (nCounter™ 'PanCancer Progression Panel'), we report that CRISPR/Cas 9-based *GLO1* deletion from human A375 malignant melanoma cells alters glucose metabolism and redox homeostasis, observable together with acceleration of tumorigenesis. Nanostring™ analysis identified *TXNIP* (encoding thioredoxin-interacting protein), a master regulator of cellular energy metabolism and redox homeostasis, displaying the most pronounced expression change in response to *GLO1* elimination, confirmed by RT-qPCR and immunoblot analysis. *TXNIP* was also upregulated in CRISPR/Cas9-engineered DU145 prostate carcinoma cells lacking *GLO1*, and treatment with MG or a pharmacological GLO1 inhibitor (TLSC702) mimicked *GLO1*_KO status, suggesting that *GLO1* controls *TXNIP* expression through regulation of MG. *GLO1*_KO status was characterized by (*i*) altered oxidative stress response gene expression, (*ii*) attenuation of glucose uptake and metabolism with downregulation of gene expression (*GLUT1*, *GFAT1*, *GFAT2*, *LDHA*) and depletion of related key metabolites (glucose-6-phosphate, UDP-N-acetylglucosamine), and (*iii*) immune checkpoint modulation (*PDL1*). While confirming our earlier finding that *GLO1* deletion limits invasion and metastasis with modulation of EMT-related genes (e.g. *TGFBI*, *MMP9*, *ANGPTL4*, *TLR4, SERPINF1*), we observed that *GLO1_KO* melanoma cells displayed a shortened population doubling time, cell cycle alteration with increased M-phase population, and enhanced anchorage-independent growth, a phenotype supported by expression analysis (*CXCL8*, *CD24*, *IL1A*, *CDKN1A*). Concordantly, an accelerated growth rate of *GLO1*_KO tumors, accompanied by *TXNIP* overexpression and metabolic reprogramming, was observable in a SCID mouse melanoma xenograft model, demonstrating that A375 melanoma tumor growth and metastasis can be dysregulated in opposing ways as a consequence of *GLO1* elimination.

1. Introduction

A majority of skin cancer-related deaths is caused by malignant melanoma, a tumor originating from neural crest-derived melanocytes, and the exploration of novel molecular strategies for improved detection and treatment of melanoma is of substantial clinical significance [1–3]. Oncometabolic adaptation is now recognized as a hallmark of melanomagenesis, and recent research has focused on metabolic rewiring involved in proliferative and metastatic dysregulation characteristic of $BRAF^{V600E}$-driven and BRAF kinase inhibitor-resistant melanoma [4,5]. Glyoxalase 1 (encoded by *GLO1;* NM_006708) is a glutathione-dependent enzyme involved in the detoxification of the reactive glycolytic byproduct methylglyoxal (MG) based on formation of (R)-S-lactoyl-glutathione from MG and reduced glutathione [6,7]. Cumulative evidence supports a crucial role of *GLO1* expression in maintaining oncometabolic adaptations as observed in the context of tumor-associated aerobic glycolysis, commonly referred to as 'the Warburg effect', facilitating survival under hypoxic conditions and enabling escape from energy crisis and apoptosis [8–10]. Substantiating a role of *GLO1* in metabolic reprogramming, cumulative research

* Corresponding author.
E-mail address: wondrak@pharmacy.arizona.edu (G.T. Wondrak).

https://doi.org/10.1016/j.redox.2020.101838
Received 15 October 2020; Received in revised form 29 November 2020; Accepted 2 December 2020
Available online 17 December 2020

has focused on the emerging role of MG [and (R)-S-lactoylglutathione] as cellular oncometabolites, involved in tumorigenesis-associated proliferative control, redox dysregulation, epigenetic recoding, and regulation of EMT, cellular functions that have been attributed to posttranslational MG-adduction of specific target proteins including histones [8,9,11–16]. Importantly, numerous malignancies (including those of the breast, colon, liver, lung, prostate, skin, stomach, and thyroid) have now been associated with a causative role of *GLO1* dysregulation, and beyond serving as a prognostic factor of patient survival, development of pharmacological and genetic strategies targeting cancer cells through GLO1 modulation has attracted significant attention [10,16–24].

Previously, using cell culture models (comparing primary melanocytes and malignant melanoma lines) as well as patient samples in tissue microarray format, we have documented that *GLO1* is overexpressed during melanoma progression [25]. Moreover, employing CRISPR/Cas 9-based *GLO1* deletion and rescue expression, we have documented a novel role of *GLO1* as a molecular determinant of invasion and metastasis observable in experimental human malignant melanoma *in vitro* and *in vivo*, a finding consistent with independent evidence indicating *GLO1*-control of prostate carcinoma cell EMT and metastatic behavior [22,26].

Here, in order to examine the consequences of genomic deletion of *GLO1* in human melanoma cells more comprehensively, we have performed NanoString™ gene expression profiling (using the nCounter™ 'PanCancer Progression' Panel) complemented by phenotypic analysis performed *in vitro* and *in vivo*. We report for the first time that genomic *GLO1* deletion modulates *TXNIP* expression, glucose metabolism, and redox homeostasis while accelerating human A375 malignant melanoma tumor growth.

2. Materials and methods

Chemicals: All chemicals were purchased from Sigma Aldrich (St. Louis, MO, USA) including MG (M0252), 2-[N-(7-nitrobenz-2-oxa-1,3-diazol-4-yl) amino]-2-deoxy-D-glucose (2-NBDG) (72987), and GLO1-inhibitor TLSC702 (ENAH5802E9A2).

Melanoma and prostate carcinoma cell culture: Human malignant A375 melanoma cells (CRL-1619; ATCC, Manassas, VA) and engineered isogenic variants {CRISPR/Cas9-derived *GLO1*_KO cells (A375 *GLO1*_KO [B40]; A375 *GLO1*_KO [C2])} were cultured in RPMI medium (Corning Inc., Corning, NY), supplemented with 10% FBS and 2 mM L-glutamine. Human DU145 prostate carcinoma cells (ATCC, HTB-81) and engineered isogenic variants {CRISPR/Cas9-derived *GLO1*_KO cells (DU145 *GLO1*_KO [A16]; DU145 *GLO1*_KO [A29])} were cultured in EMEM (Corning Inc., Corning, NY), supplemented with 10% FBS and 2 mM L-glutamine. Cells were maintained in a humidified incubator (37 °C, 5% CO_2 and 95% air).

CRISPR/Cas9-based engineering of *GLO1*_KO A375 malignant melanoma and *GLO1*_KO DU145 prostate carcinoma cells: Homozygous *GLO1* gene knock-out in human malignant A375 melanoma cells was performed using genetic engineering as published before [26]. Likewise, DU145 prostate carcinoma *GLO1*_KO cells were engineered using a similar approach (supplemental data; Fig. S1). Briefly, double strand breaks were generated on both sides of exon 2 (chromosome 6, positions: 38, 687, 313 bp; 38,685,738 bp) with guide CRISPR RNAs (5′-ACCCTCATGGACCAATCAGT-3′ and 5′-TGATCATAGGTGTATACGA G-3′). Parental cells were transfected with Cas9 protein, crRNAs, and *trans*-activating crRNA (Integrated DNA Technologies, San Diego, CA) using the Lipofectamine RNAiMAX reagent (Thermo Fisher Scientific, Waltham, MA). Next, single cells were deposited in 96-well plates and once single cell colonies expanded (after approximately three weeks), individual clones were screened by PCR. Clones that were negative for a sequence inside the targeted deletion and negative for the undeleted chromosomal sequences but positive for ligation-junction fragment were scored as potentially homozygous for *GLO1* exon 2 deletion. Absence of *GLO1* expression was confirmed by single RT-qPCR, immunoblot, and enzymatic activity assays.

***GLO1* rescue expression construct:** CMV-driven *GLO1* re-expression (A375-*GLO1*_R) in a KO clone (A375 *GLO1*_KO [B40]) was performed and validated following our previously published methodology [26]. Briefly, stable A375-*GLO1* rescue cells (A375-*GLO1*_R) were generated by overnight incubation of A375-*GLO1*_KO cells with DNA (4 μg)-Lipofectamine® 2000 (10 μg) complexes at 37 °C. After 24 h transfection, cells were passaged at 1:10 dilution into fresh growth medium. Selection antibiotic, neomycin (500 μg/ml), was added to the growth media 24 h later to select for single-cell colonies. Individual single-cell colonies were then expanded, and cells were tested for *GLO1* mRNA and protein expression.

NanoString nCounter™ gene expression analysis: The NanoString nCounter™ technology is a direct digital detection system enabling multiplexed quantification of gene expression (740 target plus 30 housekeeping genes) that occurs without amplification using fluorescent probes that bind directly to chosen mRNA targets [27,28]. First, total mRNA was prepared using RNeasy Mini kit (Qiagen, Valencia, CA) and then 100 ng used for NanoString nCounter™ analysis (using the 'PanCancer Progression Panel', NanoString Technologies, Seattle, WA) comparing gene expression between wildtype human A375 malignant melanoma cells and the isogenic *GLO1*_KO [B40] variant. Total mRNA was hybridized with the 'PanCancer Progression' code set at 65 °C overnight. Further purification and binding of the hybridized probes to the optical cartridge was performed on the nCounter™ Prep Station, and finally the cartridge was scanned on the nCounter™ Digital Analyzer. RCC files were then imported into nSolver4.0 software (NanoString Technologies) and checked for data quality using default QC settings; all samples passed data quality QC. All samples were normalized using the geometric mean of the housekeeper genes. Expression ratios were calculated by dividing the mean values of all samples in one experimental group (*GLO1*_KO) by the mean values of all samples in the reference group (*GLO1*_WT). For 'pathway score analysis' each sample's gene expression profile was then condensed into a small set of pathway scores using nCounter™ Advanced Analysis software (version 2.0.115). Pathway scores were fit using the first principal component of each gene set's data, oriented such that each pathway score has positive weights for at least half its genes. Numerical pathway score represents average fold expression change (log2 scale) for all genes associated with the specific pathway, with positive scores indicating enhancement and negative scores indicating attenuation. A 'covariate plot' displays selected pathway scores against the covariate chosen (i.e. *GLO1* genotype).

Comparative human Oxidative Stress Plus RT^2 Profiler™ gene expression array analysis: Total mRNA from cultured cells (200,000 in 35 mm dish format) was prepared using the RNeasy Mini kit (Qiagen) following our published standard procedures [26,29]. Reverse transcription was then performed using the RT^2 First Strand kit (Qiagen) from 500 ng total RNA. For gene expression array analysis, the human Oxidative Stress Plus RT^2 Profiler™ technology (Qiagen) assessing expression of 84 redox regulatory genes was used as published before [26]. Quantitative PCR was run using the following conditions: 95 °C (10 min), followed by 40 cycles at 95 °C (15 s) alternating with 60 °C (1 min) (Applied Biosystems, Carlsbad, CA). Gene-specific products were normalized to a group of 5 housekeeping genes (*ACTB*, *B2M*, *GAPDH*, *HPRT1*, *RPLP0*) and quantified using the comparative ΔΔCt method (ABI Prism 7500 sequence detection system user guide).

Single RT-qPCR analysis: Total RNA was isolated using the Qiagen RNeasy Mini Kit (Qiagen) according to the manufacturer's protocol. RNA integrity was checked by the RNA 6000 Nano chip kit using Agilent 2100 Bioanalyzer (Agilent Technologies, Santa Clara, CA). Human 20X primer/probes [*GLO1* (Hs_02861567_m1), *GLO2* (Hs_00193422_m1), *TXNIP* (Hs_01006900_m1), *SLC2A1* (Hs_00892681_m1), *CDKN1A* (Hs_00355782_m1), *GFPT1* (Hs_00157686_m1), *GFPT2* (Hs_01049570_m1), *PD-L1* (Hs_00204257_m1), *MMP9* (Hs_00234579_m1), *TXNRD2*

(Hs_01561341_m1), *SRXN1* (Hs_00607800_m1), *GSTZ1* (Hs_01041668_m1), *HMOX1* (Hs_00157965_m1), *RPS18* (housekeeping gene; Hs_01375212_g1)] were obtained from Thermo Fisher Scientific, Waltham, MA. 500 ng of total RNA was used for cDNA synthesis using following cycling conditions: 25 °C for 10 min; 48 °C for 30 min and 95 °C for 5 min performed in MJ Thermocycler PTC-200 (MJ Research, Watertown, MA). Then, 10 ng of cDNA was used for amplification of target genes by quantitative PCR using following conditions: 95 °C for 10 min followed by 95 °C for 15 s and 60 °C for 1 min for a total of 40 cycles performed in the ABI7500 Real-Time PCR System (Applied Biosystems, Foster City, CA). PCR amplification of human housekeeping gene *RPS18* was used to control quality of the cDNA. Non-template controls were included on each PCR plate. Expression levels of target genes were normalized to the *RPS18* control [ΔCt = Ct (gene of interest) – Ct (housekeeping gene)]. Amplification plots were generated and the Ct values (cycle number at which fluorescence reaches threshold) recorded as published before [26,30].

Immunoblot analysis: After cellular protein extraction using RIPA buffer (50 mM Tris, pH 7.4, 150 mM NaCl, 1 mM EDTA, 1% Triton N-100, 1% sodium deoxycholate and 0.1% sodium dodecyl sulfate) supplemented with protease inhibitor mixture (leupeptin, aprotinin, PMSF), equal amounts of total protein were separated using 4%–15% SDS-PAGE gel (Bio-Rad laboratories, Irvine, CA) transferred to PVDF membrane, and developed. Detection of proteins was conducted using the following primary antibodies: p21 Waf1/Cip1 (2947, Cell Signaling, Danvers, MA); PD-L1 (13684, Cell Signaling); GFPT1 (ab25069, Abcam, Cambridge, MA); GLO1 (ab96032, Abcam) and TXNIP (NBP2-75692, Novus Biologicals, Centennial, CO). The following secondary antibodies were used: HRP-conjugated goat anti-rabbit antibody or HRP-conjugated goat anti-mouse antibody (Jackson ImmunoResearch Laboratories, West Grove, PA, USA). Membranes were incubated with ECL Western Blotting Detection Reagents (Amersham Biosciences, Piscataway, NJ) and exposed to BioMax XAR film (Kodak, Rochester, NY). Equal protein loading was examined by β-actin detection using a mouse anti-actin monoclonal antibody (Sigma Aldrich, St. Louis, MO, USA). For quantification, densitometric image analysis was performed using Image Studio™ Lite quantification software (LI-COR Biosciences, Lincoln, NE) [26,31].

MMP9 ELISA: Quantikine™ MMP9 ELISA (PDMP900; R&D Systems, Minneapolis, MN) was used to measure the 92 kDa Pro- and 82 kDa active forms in cell culture supernatants of parental A375 cells and their *GLO1* isogenic variants. Briefly, supernatants were collected, and samples prepared by removing particulates by centrifugation. Then, 100 μL of standards, controls, and 100-fold diluted supernatant samples were added to 100 μL of assay diluent in MMP9 pre-coated wells followed by ELISA procedure as specified by the manufacturer. Colorimetric analysis (450 nm) was performed using a BioTek Synergy 2 Reader (BioTek, Winooski, VT). Results were normalized to total sample protein using the Pierce™ BCA Protein Assay Kit (Thermo Fisher Scientific, Waltham, MA, USA) [26].

Cell proliferation assay and population doubling time: Cells (1,000 per 35 mm dish) were seeded followed by culture in fresh growth medium (72 h). Viable cells (as determined by trypan blue exclusion assay) were counted (d0 and d3) using a Cell Viability Analyzer (Beckman Coulter, Fullerton, CA, USA). Population doubling time (DT) was then calculated as follows: $DT = T \times \ln 2 / \ln (X_e/X_b)$ [T is the incubation time (72 h), X_b is the cell number at the beginning of the incubation time, and X_e is the cell number at the end of the incubation time] [26].

Cell cycle analysis: Cells were harvested by trypsinization, resuspended in 200 μl PBS, and placed on ice. After addition of 2 ml 70% (v/v) ethanol, 30% (v/v) PBS, cells were incubated for 30 min on ice. The fixed cells were pelleted by centrifugation, resuspended in 800 μl PBS, 100 μl ribonuclease A (1 mg/ml PBS), and 100 μl propidium iodide (PI, 400 μg/ml PBS), and incubated for 30 min in the dark at 37 °C. Cellular DNA content was determined by flow cytometry and analyzed using the ModFit LT software, version 5.0 (Verity, Topsham, ME, USA) [31,32].

M-phase quantification by phospho-histone H3 (Ser10) flow cytometry: Cells in M-phase were detected by bivariate flow cytometric determination of cellular DNA content (PI-staining) and histone H3 phosphorylated at Ser 10 [p-H3(Ser10)] using a rabbit derived Alexa-488 conjugated antibody (Cell Signaling, Inc., Danvers, MA, USA) according to the manufacture's protocol. p-H3(Ser10)-positive cells in M-phase were expressed in percent of total gated cells [32].

Glucose-metabolite analysis by UPLC-MS analysis: Sugar phosphate analysis was performed as published recently [33,34]. For UPLC-MS (ultra-performance liquid chromatography), a Dionex 3400 UHPLC system coupled to a 4000 QTRAP mass spectrometer was used. The MS instrument was operated in the multiple-reaction monitoring (MRM) mode with negative- or positive-ion detection. For quantification of selected sugar phosphates [glucose-6P (Glc-6P), glucosamine-6P (GlcN-6P), NAc-glucosamine-6P (GlcNAc-6P), ribose-5P (R–5P), ribulose-5P (Ru–5P)], each cell pellet was redissolved in 250 μL of 80% aqueous methanol. The cell sample was then sonicated in an ice-water bath for 5 min and vortexed for 15 s, followed by centrifugation (15, 000 rpm, 5 °C, 15 min). The supernatant was collected, and the protein pellet was used for BCA protein assay. For quantification of sugar phosphates, 50 μL of each supernatant and standard solutions containing stable-isotope-labeled internal standard (such as $^{13}C_6$-glucose-6P) were mixed with 50 μL of 25 mM AEC (3-amino-9-ethylcarbazole) solution, followed by addition of 100 μL of 50 mM $NaBCNH_3$ solution and 20 μL of acetic acid. The mixtures were allowed to react at 60 °C (70 min). After reaction, 300 μL of water and 300 μL of chloroform were added to each tube. The mixtures were vortexed followed by centrifugation (10,000 rpm; 10 min). The aqueous phase was then subjected to UPLC-MS analysis. For nucleotide [UDP-N-acetylglucosamine (UDP-GlcNAc)] analysis, C18-UPLC with gradient elution [ammonium tributylamine buffer (mobile phase A) and acetonitrile (mobile phase B); 15% B to 60% B over 20 min] was performed followed by negative ion MS detection.

Glucose uptake by flow cytometry: Cells (100,000/well) were seeded in a 6-well plate. After overnight incubation in normal growth media, cells were incubated in glucose-free medium for 10 min (37 °C, CO_2 incubator). Then, glucose free media was replaced with HBSS supplemented with 2-NBDG (300 μM). After 10 min incubation (37 °C), cells were collected, washed twice in PBS, and analyzed by flow cytometry (FITC channel; Ex/Em 485/535 nm) [35].

Cellular oxygen consumption and extracellular acidification rates: Oxygen consumption rate (OCR) and extracellular acidification rate (ECAR) were measured using the XF^{e}96 Analyzer (Agilent, Santa Clara, CA) according to manufacturer's instructions as published by us before [36]. Briefly, 30,000 cells per well were seeded in the XF tissue culture plate in normal growth media. The cartridge was hydrated by adding 200 μL of calibrant solution to each well and incubated overnight in a 37 °C non-CO_2 incubator. After cartridge calibration, the cell culture plate was processed followed by data collection. For OCR, cells were washed with XF Cell MitoStress Test Assay Media containing unbuffered DMEM (4.5 g/L glucose; 1 mM sodium pyruvate; pH 7.4) using the XF Prep Station, followed by incubation (1 h) in the prep-station non-CO_2 incubator. Port A of the cartridge was then loaded with 25 μL of the mitochondrial uncoupler FCCP (1 μM).

Luminescent ATP assay: Cells were seeded at 50,000 cells/dish on 35-mm dishes. After 24 h, cells were harvested and counted, and ATP content per 10,000 cells was determined using the CellTiter-Glo™ luminescent assay (Promega, Madison, WI, USA) in 96 well format according to the manufacturer's instructions. Data are normalized to ATP content in untreated cells [26,32].

Detection of intracellular oxidative stress: Induction of intracellular oxidative stress by MG was analyzed by flow cytometry using 2′,7′-dichlorodihydrofluorescein diacetate (DCFH-DA) as a sensitive non-fluorescent precursor dye according to a published standard procedure [26,37]. Cells were treated with MG (500 μM, 6 h), followed by DCFH-DA loading. Cells were incubated for 60 min in the dark (37 °C, 5% CO_2) with culture medium containing DCFH-DA (5 μg/ml). Cells

were then harvested and analyzed immediately by flow cytometry.

Determination of reduced cellular glutathione content: Intracellular reduced glutathione was measured using the GSH-Glo™ Glutathione assay kit (Promega; San Luis Obispo, CA) [26,30,37]. Cells were seeded at 100,000 cells/dish on 35 mm dishes. After 24 h, cells were harvested by trypsinization and then counted using a Coulter counter. Cells were washed in PBS, and 10,000 cells/well (50 μL) were transferred onto a 96-well plate. GSH-Glo reagent (50 μL) containing luciferin-NT and glutathione-S-transferase was then added followed by 30 min incubation. After addition of luciferin detection reagent to each well (100 μL) and 15 min incubation luminescence reading was performed using a BioTek Synergy 2 Reader (BioTek, Winooski, VT).

Transwell invasion assay: Matrigel-coated 8 μm pore size translucent 24-well plate transwell chambers (BD Biosciences, San Jose, CA) were used to evaluate the invasion potential of A375 cells following a published standard procedure [26]. Briefly, 600 μL of normal growth medium (10% FBS) was added to the bottom of each well and a total of 2.5×10^4 cells resuspended in 250 μL of invasion buffer (normal growth medium; 0.5% FBS; 0.1% BSA) were seeded on top. After 24 h incubation at 37 °C, 5% CO_2, non-invading cells were removed by wiping the upper side of the membrane, and invading cells fixed with methanol and stained with crystal violet (Sigma-Aldrich, St. Louis, MO, USA). The number of invading cells was quantified by counting 10 random fields per filter at 400 × magnification.

Anchorage-independent growth on soft agar: Agar (3% in sterile water) was autoclaved, kept at 48 °C on a water bath and diluted using normal growth media (0.6% final concentration), and then poured on a 6-well plate and solidified at room temperature. After solidification of the bottom layer, a top layer was prepared (0.3% final agar concentration containing 20,000 cells). The plate was then incubated for 14 days in a cell culture incubator. During this period, cells were fed with normal growth media. At the end of the experiment, plates were fixed and stained with crystal violet (0.005%). Individual colonies (larger than 70 μm) were counted using light microscopy [38].

Metastasis model in SCID mice: A375 and its *GLO1*_KO isogenic variants (WT, *GLO1*_KO) were inoculated with 1×10^6 cells resuspended in 100 μL HBSS using intravenous (i.v.) tail vein injection of SCID mice. The mice (n = 5 per group) were obtained from the University of Arizona Cancer Center SCID house colony at the age of 9 weeks with an average weight of 20 g. At the end of the experiment (21 d post injection), lungs were evaluated for presence and number of metastases, and tissues fixed in NBF. This study was performed in accordance with the recommendations of the National Institutes of Health (University of Arizona Institutional Animal Care and Use Committee; mouse protocol number: IACUC 17–298) [26].

Human A375 melanoma SCID mouse xenograft model: A SCID mouse colony was developed at the University of Arizona using original SCID (C·B-17/IcrACCSCID) obtained from Taconic (Germantown, New York). The mice were housed in microisolator cages (Allentown Caging Equipment Company, Allentown, N.J.) and maintained under specific pathogen-free conditions. The mice received NIH-31 irradiated pellets (Tekland Premier, Madison, WI) and autoclaved water. Animal facilities are approved by the Association for the Assessment and Accreditation of Laboratory Animal Care International and in accordance with United States Department of Agriculture, Department of Health and Human Services, and NIH regulations. A375 melanoma cells (1×10^6/100 μL HBSS) were injected subcutaneously (lower right flank) on day 0 (n = 10 per genotype). Tumor growth curves were generated by monitoring average tumor volumes (mm^3) until day 28 after cell injection followed by tumor collection. All procedures were completed in accordance with the University of Arizona Institutional Animal Care and Use Committee (IACUC) protocol (IACUC 17–298). Specific tumor growth rate (SGR) was determined between day 6 (last time point of equal average tumor growth between groups) and day 28 (end of experiment with final tumor measurement) as follows: $SGR = \ln (V_2/V_1)/(t_2 - t_1)$, where V_1 and V_2 are the tumor volumes at day 6 (t_1) and day 28 (t_2), respectively [39].

Immunohistochemistry: After tumor collection, tissue was fixed in 10% NBF and processed for paraffin embedment. Sections from each tissue block were counterstained with hematoxylin/eosin and analyzed for antigen detection: GLO1 (CPTC-GLO1-1; DSHB, Iowa City, IA), TXNIP (NBP2-75692, Novus Biologicals), SLC2A1 (GLUT1; ab40084, Abcam), GFPT1 (ab25069, Abcam), p21 (2947, Cell Signaling; 1:50), PD-L1 (13684, Cell Signaling), and Ki67 (ab15580, Abcam) following our published procedures [26,31]. In brief, following deparaffinization and hydration, slides were washed and subjected to citric (pH 6.0)/Tris-EDTA (pH 9.0) heated antigen retrieval. Slides were then incubated with primary antibody. After overnight incubation, slides were washed and incubated with anti-mouse/anti-rabbit secondary antibody, washed and then incubated with the streptavidin/horseradish peroxidase (RTU PK7200, Vector Laboratories, Burlingame, CA, USA). Slides were developed with a diaminobenzidine/hydrogen peroxide mixture (Vectastain ABC, SK-4103, Vector Laboratories), counterstained with hematoxylin, dehydrated with graded alcohols and xylene, and mounted using a xylene based medium. Negative controls were performed on each run, substituting the primary antibody with mouse IgG1 (X0931, Agilent/DAKO, Santa Clara, CA, USA). Images were captured using an Olympus BX50 and Spot (Model 2.3.0) camera.

Statistical analysis: Unless stated differently, data sets were analyzed employing analysis of variance (ANOVA) with Tukey's posthoc test using the Prism 8.4.3 software (Prism Software Corp., Irvine, CA); in respective bar graphs (analyzing more than two groups), means without a common letter differ ($p < 0.05$). For bar graphs comparing two groups only, statistical significance was calculated employing the Student's two-tailed *t*-test, utilizing Excel (Microsoft™, Redmond, WA). The level of statistical significance was marked as follows: $*p < 0.05$. Experiments involved at least nine individual replicates per data point, except for gene expression array analysis performed with three independent biological replicates analyzed in triplicate format. For NanoString nCounter™ expression profiling, individual samples were run in triplicate format of biological replicates, and data analysis was performed using the nSolver analysis software (4.0). For p-value adjustment (Benjamini-Yekutieli False Discovery Rate; p value threshold: 0.05) nCounter™ Advanced Analysis software (version 2.0.115) was used. Nonparametric data analysis of murine experimentation was performed using the Mann–Whitney test. Differences between groups were considered significant at $*p < 0.05$.

3. Results

NanoString™ gene expression and cancer pathway analysis identifies pronounced *TXNIP* upregulation as a consequence of CRISPR/Cas9-based *GLO1* deletion in human A375 malignant melanoma cells.

First, in order to assess consequences of genomic deletion of *GLO1* in human melanoma cells, NanoString™ nCounter™ analysis (using the 'PanCancer Progression' panel) was performed, comparing gene expression between cultured human A375 malignant melanoma cells and an isogenic *GLO1*_KO variant (B40_KO) as engineered by us before (Fig. 1) [26]. Out of 740 genes monitored, 141 genes displayed expression changes with a statistically relevant change as a function of *GLO1*_KO genotype, depicted as a volcano plot [fold change over p-value (Fig. 1a)], heat map [fold change ≥ 2 (Fig. 1b, left panel)], and tabular summary of statistically significant gene expression changes [fold change ≥ 2 (Fig. 1c, right panel)]. Genes displaying upregulated expression by at least 4-fold were identified as *TXNIP* (14.1-fold), *IL1A* (9.6-fold), *CD24* (9.3-fold), *CXCL8* (5.2-fold), *SERPINF1* (4.7-fold), and *FSTL1* (4.0-fold). Genes displaying downregulated expression by at least 4-fold were identified as *TGFBI* (5.9-fold), *MMP9* (5.2-fold), *CTSK* (4.7-fold), and *ANGPTL4* (4.7-fold).

Using nCounter™ Advanced Analysis software, 'pathway score' profiling identified a number of gene expression networks, characterized by differential expression patterns as a function of *GLO1*_KO status (Fig. 1c). Among these, four out of six networks were characterized by

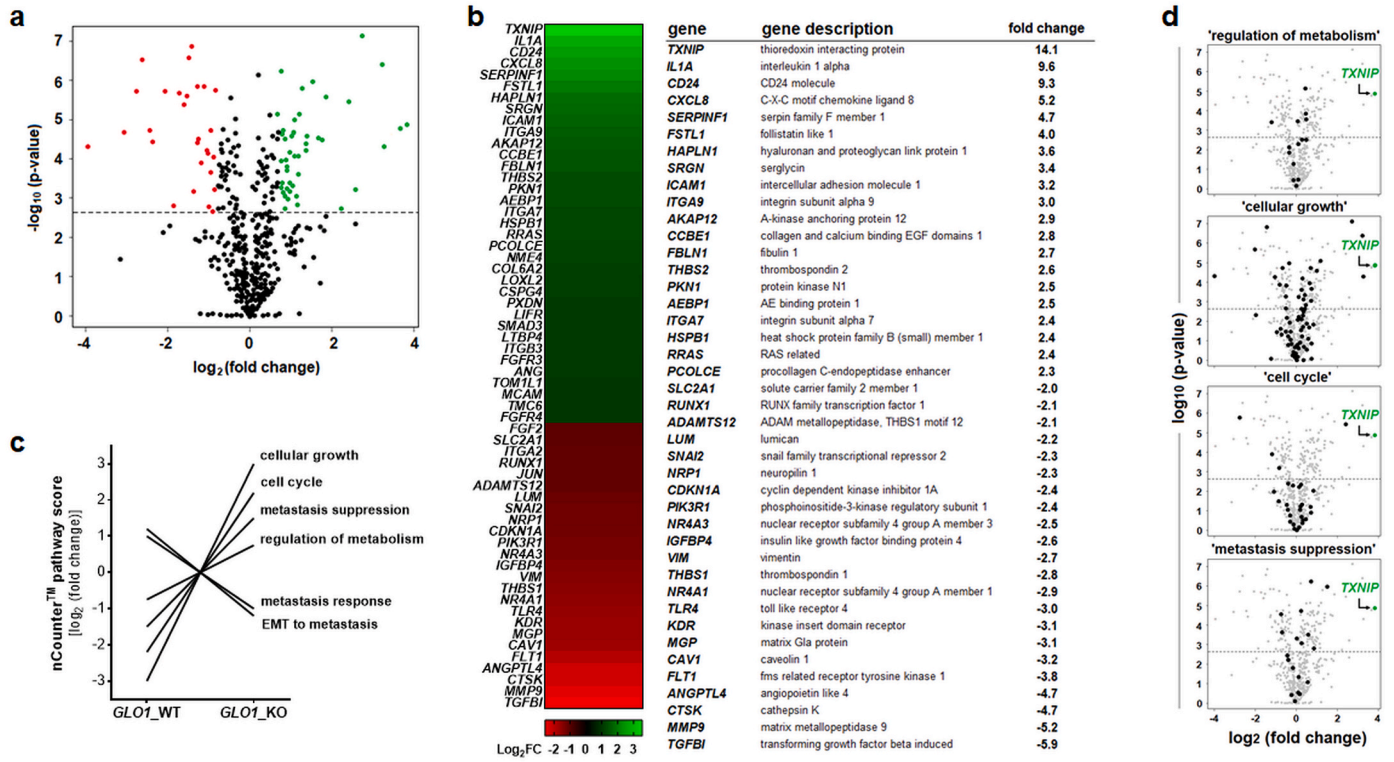

Fig. 1. NanoString nCounter™ profiling identifies pronounced gene expression changes (including *TXNIP* upregulation) as a consequence of CRISPR/Cas9-based *GLO1* deletion in human A375 malignant melanoma cells. NanoString™ analysis (using the nCounter™ PanCancer Progression Panel) was performed comparing gene expression between cultured human A375 malignant melanoma cells (*GLO1*_WT) and an isogenic variant (*GLO1*_KO [B40]). (a) Volcano plot [fold change (log2) versus p-value (log10)] depicting differential gene expression of 740 genes (*GLO1*_KO versus *GLO1*_WT; cut-off criteria: fold change ≥ 2; $p \leq 0.05$; upregulated: green dots; downregulated: red dots). (b) Left panel: heat map depiction of statistically significant expression changes; right panel: table summarizing numerical values of up- and downregulated genes; cut off criteria as specified in (a). (c) NanoString nCounter™ covariate plot of gene expression 'pathway scores' as a function of *GLO1* genotype identifying *GLO1*-responsive expression networks. (d) Volcano plots depicting individual expression pathways identified in panel (c) characterized by *TXNIP* upregulation representing the most pronounced expression change: 'regulation of metabolism' (out of 16 genes), 'cellular growth' (out of 97 genes), 'cell cycle' (out of 46 genes), and 'metastasis suppression' (out of 19 genes). (For interpretation of the references to colour in this figure legend, the reader is referred to the Web version of this article.)

upregulation of *TXNIP* [encoding 'thioredoxin-interacting protein'; also known as *VDUP1* (Vitamin D3 up-regulated protein 1)], representing the most pronounced gene expression change elicited by *GLO1* deletion: (*i*) 'regulation of metabolism', (*ii*) 'cellular growth', (*iii*) 'cell cycle', and (*iv*) 'metastasis suppression' (Fig. 1d). In addition, two additional pathways ('*EMT to metastasis*' and 'metastasis response', attenuated in response to *GLO1*_KO) were identified by score analysis, an observation in concordance with our previously published study that documented impaired A375 melanoma cell invasion and metastasis observable upon *GLO1* deletion [26].

Therefore, our further investigations focused on networks characterized by upregulation of *TXNIP*, representing the most pronounced gene expression change associated with *GLO1* deletion as identified by NanoString nCounter™ analysis.

Genomic *GLO1* deletion upregulates *TXNIP* expression in human DU145 prostate carcinoma and A375 melanoma cells associated with attenuation of glucose uptake and metabolism in *GLO1*_KO cells.

In addition to upregulation of *TXNIP* expression, NanoString nCounter™ analysis identified other gene expression changes contributing to 'regulation of metabolism' pathway score alteration in *GLO1*_KO melanoma cells, i.e. downregulation of *LDHA* (encoding lactate dehydrogenase A) and *SLC2A1* (*GLUT1* encoding glucose transporter 1) (Fig. 1c and d and 2a). *TXNIP* expression changes (mRNA and protein levels) were also confirmed by single RT-qPCR and immunoblot analyses (A375 *GLO1*_WT versus *GLO1*_KO clones [B40 and C2]; Fig. 2b and c).

Next, we tested if *TXNIP* upregulation observable in A375 *GLO1*_KO melanoma cells is also detectable in CRISPR/Cas9-engineered DU145 *GLO1*_KO prostate carcinoma cells characterized by absence of *GLO1* expression confirmed at the mRNA and protein levels (Fig. 2d,e and supplemental Fig. S1). Indeed, pronounced upregulation of *TXNIP* expression occurred in DU145 *GLO1*_KO clones [A16 and A29] as measured at the mRNA and protein levels (Fig. 2d and e).

We also tested if two pharmacological interventions associated with a direct increase in cellular MG levels were able to mimic effects of *GLO1*_KO status on *TXNIP* expression in A375 cells (Fig. 2f). Strikingly, treatment with MG, the oncometabolite inactivated by GLO1 enzymatic turnover, as well as treatment with TLSC702, a pharmacological GLO1 inhibitor elevating cellular MG levels through blockade of MG detoxification, caused significant upregulation of *TXNIP* expression as detected by RT-qPCR [21,40]. Taken together, this evidence (obtained from genetic and pharmacological target modulation) suggests that *TXNIP* expression is responsive to *GLO1* expression status and that *GLO1* might control *TXNIP* through regulation of cellular MG levels.

Next, we explored the possibility that genetic elimination of *GLO1* in A375 malignant melanoma cells might be associated with pronounced changes affecting glucose metabolism (Fig. 3a–g). To this end, we designed experiments based on the established involvement of *GLO1* in glycolysis-associated MG-detoxification and the critical role of the tumor suppressor *TXNIP* as a key modulator of cellular glucose uptake and energy metabolism [41–43]. First, a limited number of glucose-related signature metabolites was profiled using quantitative UPLC-MRM/MS analysis of cultured human A375 cells compared to an isogenic *GLO1*_KO [B40] variant (Fig. 3a). Pronounced changes

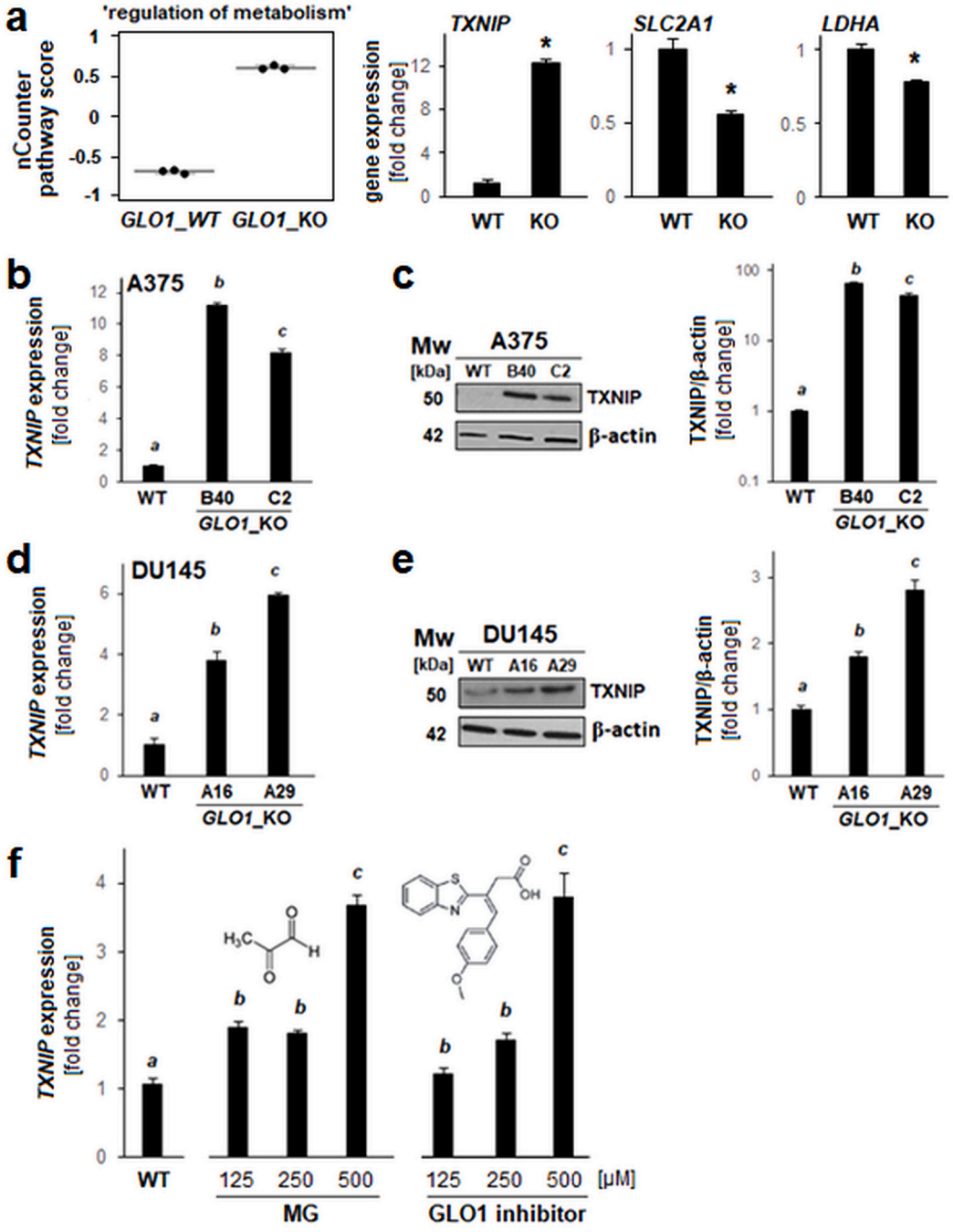

Fig. 2. Genetic deletion of *GLO1* causes upregulation of *TXNIP* expression in DU145 prostate carcinoma and A375 malignant melanoma cells, and *TXNIP* expression is sensitive to pharmacological modulation using the GLO1 inhibitor TLSC702. (a) NanoString nCounter™ pathway score analysis of 'regulation of metabolism' (box plot depiction); single panels indicate comparative metabolism-related gene expression [*TXNIP*, *SLC2A1* (*GLUT1*), *LDHA*]. (b–c) *TXNIP* expression in A375 melanoma (*GLO1*_WT versus *GLO1*_KO clones [B40 and C2]) as confirmed by independent RT-qPCR (b) and immunoblot (c) analyses; bar graph depicts immunoblot quantification over β-actin control. (d–e) *TXNIP* expression in DU145 prostate carcinoma cells (*GLO1*_WT versus *GLO1*_KO clones [A16 and A29]) as confirmed by independent RT-qPCR (d) and immunoblot (e) analyses; bar graph depicts immunoblot quantification over β-actin control. (f) *TXNIP* expression in A375 melanoma cells (*GLO1*_WT) exposed to MG-modulatory treatments [left panel: MG dose response; right panel: GLO1-inhibitor (TLSC702) dose response (24 h continuous exposure)] as confirmed by RT-qPCR analysis; molecular structures included. For all bar graph depictions, quantitative data analysis employed ANOVA with Tukey's post hoc test; means without a common letter differ from each other ($p < 0.05$). For bar graphs comparing two groups only, statistical significance was calculated employing the Student's two-tailed *t*-test (*p < 0.05).

indicative of (*i*) decreased glycolytic entry [glucose-6-phosphate (Glc-6P)], (*ii*) decreased flux through the hexosamine biosynthesis pathway (HBP) [glucosamine-6-phosphate (GlcN-6P), N-acetylglucosamine-6-phosphate (GlcNAc-6P), uridine diphosphate N-acetylglucosamine (UDP-GlcNAc)], and (*iii*) increased flux through the pentose-phosphate pathway (PPP) [ribose-5-phosphate (R–5P), ribulose-5-phosphate (Ru–5P)] were detectable.

Cellular glucose uptake was then assessed employing a flow cytometric assay that measures uptake of the fluorescent glucose probe 2-NBDG (Fig. 3b). Consistent with the glucose metabolite profile (glucose-6-phosphate) and downregulation of *SLC2A1* (*GLUT1*) described above [Figs. 2a and 3a], *GLO*1_KO status was associated with

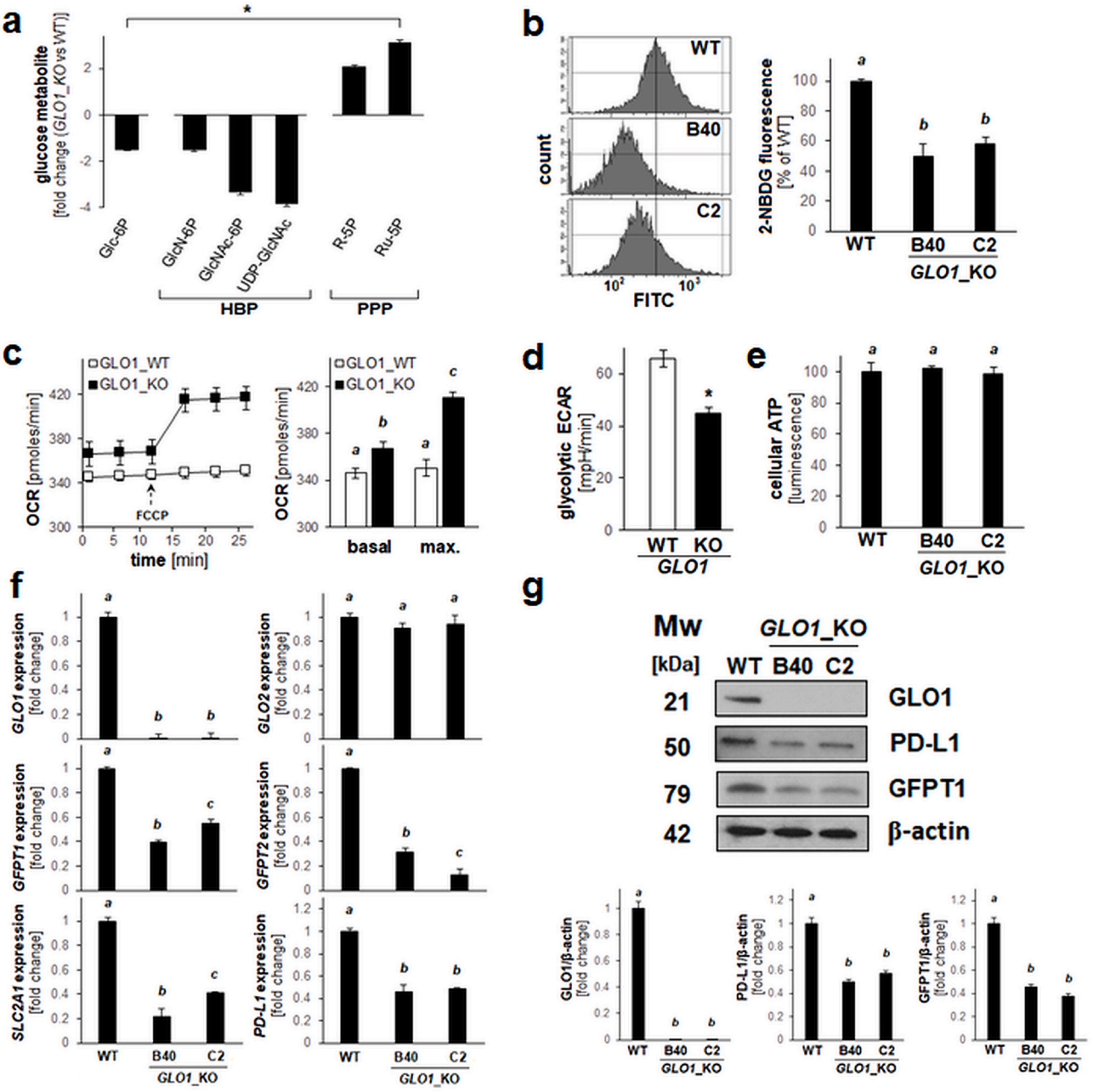

Fig. 3. Genetic deletion of *GLO1* is associated with altered glucose uptake and metabolism in human A375 melanoma cells. (a) Glucose-derived signature metabolite profiling of cultured human A375 malignant melanoma (*GLO1*_WT) versus isogenic *GLO1*_KO [B40] cells by quantitative UPLC-MRM/MS analysis (HBP: hexosamine biosynthesis pathway; PPP: pentose phosphate pathway). (b) Glucose uptake as assessed by flow cytometry using the fluorescent glucose analogue 2-NBDG. Histograms (left panels) display representative measurements; bar graph (right panel) summarizes numerical analysis. (c) Oxygen consumption rate (OCR) as determined by Seahorse™ metabolic analysis using the mitochondrial uncoupler FCCP. Image displays a representative OCR time course (left panel); bar graph summarizes numerical analysis of basal and maximal respiration (right panel). (d) Glycolytic extracellular acidification rate (ECAR) as determined by Seahorse™ metabolic analysis; bar graph summarizes numerical analysis. (e) Cellular ATP levels (normalized to cell number) as determined using CellTiter-Glo™ luminescence analysis. (f,g) Expression of glucose metabolism-related genes (including *PDL1*) as analyzed by (f) RT-qPCR and (g) immunoblot analysis of *GLO1*_WT versus *GLO1*_KO [B40 and C2] cells; bar graph summarizes immunoblot quantifications over β-actin control. For all bar graph depictions, quantitative data analysis employed ANOVA with Tukey's post hoc test; means without a common letter differ from each other ($p < 0.05$). For bar graphs comparing two groups only, statistical significance was calculated employing the Student's two-tailed *t*-test (*$p < 0.05$).

an attenuation of cellular glucose uptake detectable in two KO clones {*GLO1*_KO [B40]: 50% downregulation; *GLO1*_KO [C2]: 42% downregulation (relative to *GLO1*_WT); Fig. 3b}. Strikingly, oxygen consumption rates (OCR) as determined by metabolic flux analysis were increased significantly in *GLO1*_KO cells (Fig. 3c). Specifically, under conditions of chemical uncoupling (using FCCP), maximum mitochondrial oxygen consumption was increased by almost 15% in KO as compared to WT cells, and a small yet significant increase of basal oxygen consumption by approximately 5% was detectable in KO cells. Concordantly, KO cells displayed an approximately 30% reduction in extracellular acidification rate (ECAR) as compared to the isogenic wildtype control (Fig. 3d). At the same time, cellular ATP levels remained unchanged in KO as compared to WT cells (Fig. 3e). These observations concerning glucose uptake and metabolite profile (Fig. 3a

and b), oxygen consumption (Fig. 3c), glycolytic acidification (Fig. 3d), and ATP levels (Fig. 3e) suggest that in *GLO1*_KO cells an attenuation of glucose utilization is counterbalanced by increased mitochondrial oxygen consumption maintaining ATP levels, an observation consistent with metabolic reprogramming, a hypothesis to be tested by more detailed mechanistic experiments.

Next, guided by the observation that glucose uptake and metabolism through HBP were attenuated in *GLO1*_KO cells (Fig. 3a and b), expression of *SLC2A1* together with *GFAT1* and *GFAT2* (encoding the HBP key enzymes glutamine-fructose-6-phosphate transaminase 1 and 2, respectively) was assessed by RT-qPCR (Fig. 3f). Indeed, downregulation of *GFAT1*, *GFAT2,* and *SLC2A1* mRNA expression was observable in *GLO1*_KO cells [B40 and C2] (displaying the characteristic absence of detectable *GLO1* with unchanged *GLO2* mRNA levels). Immunoblot analysis confirmed this observation at the protein level (Fig. 3g).

Finally, since tumor glucose metabolism (as associated with high flux through glycolysis and the hexosamine pathway) has recently been shown to modulate expression of specific genes relevant to cancer cell immune evasion, we focused on expression of *PDL1*, an important endogenous immunosuppressive mediator expressed by melanoma cells (including cultured A375; Fig. 3f and g) [44–48]. Indeed, we observed that *PDL1* expression (*GLO1*_WT versus *GLO1*_KO [B40 and C2]) was attenuated as a consequence of *GLO1*_KO status, both at the mRNA and protein levels, a remarkable observation given the importance of PD-L1 as a crucial target for clinically relevant melanoma immunotherapeutic intervention.

Genomic deletion of *GLO1* alters oxidative stress response gene expression in human A375 malignant melanoma cells.

*GLO1*_KO clones were also profiled for alteration of redox stress response gene expression, an analysis guided by the established role of *TXNIP* as an antagonistic modulator of thioredoxin function and key regulator of cellular redox homeostasis [49,50]. To this end, since only a limited number of redox-directed genes (including *TXNIP*) was interrogated by our NanoString nCounter™ 'PanCancer Progression' Panel, comparative human Oxidative Stress Plus RT^2 Profiler™ gene expression array analysis was performed with *GLO1*_WT and *GLO1*_KO [B40 and C2] cells (Fig. 4a–d). Pronounced modulation of redox-related gene expression as a function of *GLO1* deletion was detected, shown by volcano and heat map depiction (Fig. 4a–b). In both *GLO1*_KO clones, out of 84 genes, 17 displayed upregulation and 13 downregulation by more than two-fold (Fig. 4c). Between KO clones, gene-specific changes (relative to WT control) occurred with comparable magnitude, 12 of which are featured in bar graph format (Fig. 4d).

Specifically, expression of *TXN* (encoding thioredoxin), an established consequence of increased *TXNIP* expression, displayed pronounced downregulation in *GLO1*_KO clones (Fig. 4b–d) [41]. Moreover, expression of genes encoding thioredoxin-regenerating enzymes was changed dramatically, with *TXNRD1* (encoding cytosolic thioredoxin reductase 1) and *TXNRD2* (encoding mitochondrial thioredoxin reductase 2) displaying pronounced down- or upregulation, respectively. Likewise, genes encoding thioredoxin-dependent antioxidant enzyme systems of the peroxiredoxin class displayed significant expression changes (up-regulated: *PRDX2*, *PRDX5*; down-regulated:

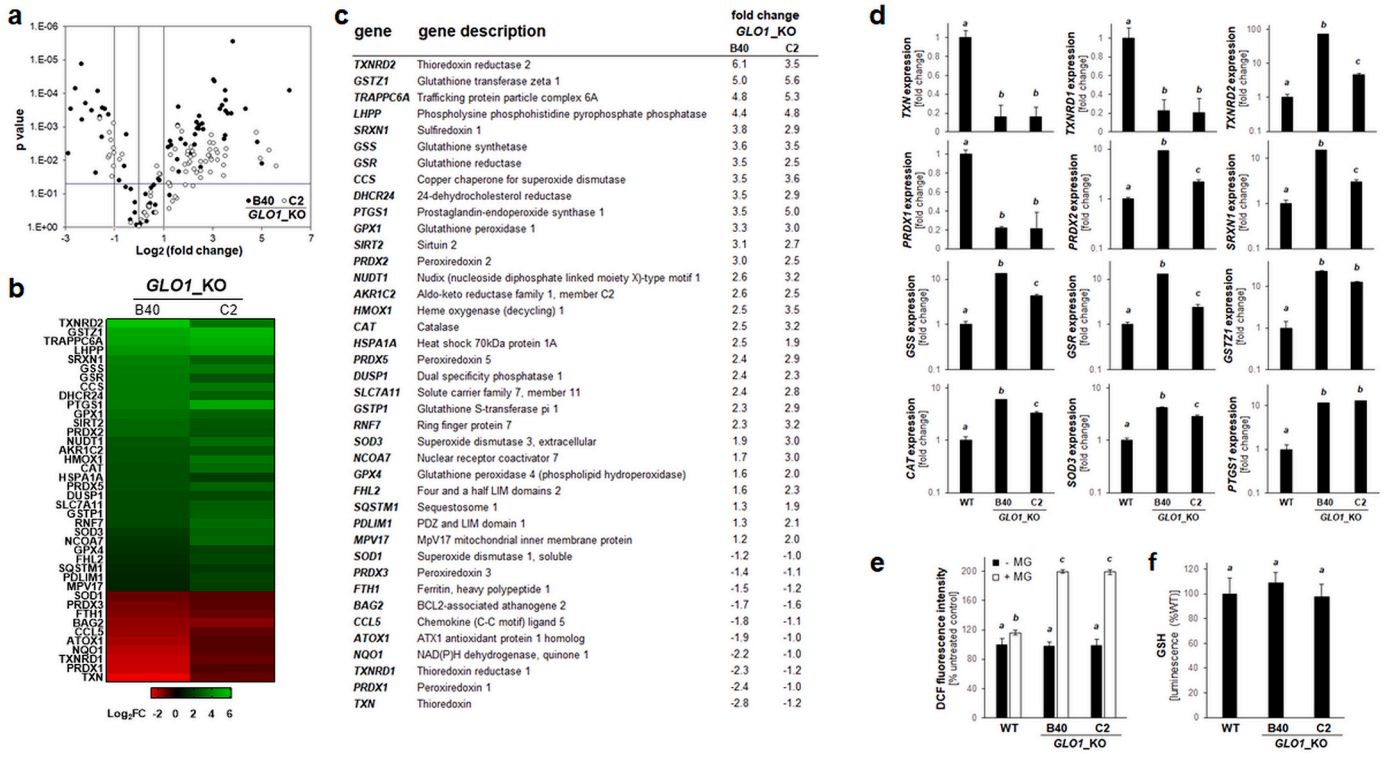

Fig. 4. Genetic deletion of *GLO1* alters redox stress response gene expression in human A375 melanoma cells. (a) RT^2 Profiler™ PCR array analysis of redox stress response genes expression (*GLO1*_KO clones [B40 and C2] relative to *GLO1*_WT). Volcano plot depicts differential gene expression (cut-off criteria: expression differential ≥ 2; p value ≤ 0.05; filled circles: *GLO1*_KO [B40]; empty circles: *GLO1*_KO [C2]). (b–c) Heat map depiction of statistically significant expression changes (log2 fold change) revealing clustered modulation of redox-related genes as a function of *GLO1* deletion [as summarized numerically in (c)]. (d) *GLO1*-modulated 'oxidative stress response' as revealed at the single gene expression level (*GLO1*_WT versus *GLO1*_KO clones [B40 and C2]): thioredoxin-related: *TXN*, *TXNRD1*, *TXNRD2*, *PRDX1, PRDX2*; glutathione-related: *GSS*, *GSR*, *GSTZ1*; other antioxidant factors: *SRXN1*, *CAT*, *SOD3*; inflammation: *PTGS1*. Bar graphs depict fold change (logarithmic or metric scale according to data range). (e) Oxidative stress (*GLO1*_WT versus *GLO1*_KO clones [B40 and C2]) as monitored by flow cytometric detection of DCF fluorescence [with or without MG treatment (500 μM, 2h)]. (f) Intracellular reduced glutathione content as assessed by luminescence intensity (GSH-Glo™) normalized to cell number (*GLO1*_WT versus *GLO1*_KO clones [B40 and C2]). For all bar graph depictions, quantitative data analysis employed ANOVA with Tukey's post hoc test; means without a common letter differ from each other ($p < 0.05$).

PRDX1, *PRDX3*).

Also, displaying consistent overexpression as a function of *GLO1*_KO status, pronounced upregulation of *SRXN1* (encoding sulfiredoxin, an enzyme involved in reductive regeneration of hyper-oxidized peroxiredoxins) was observed (Fig. 4b–d). Likewise, in *GLO1*_KO clones, expression of numerous key antioxidant factors involved in glutathione metabolism (i.e. synthesis, reductive regeneration, and electrophilic detoxification) was upregulated, including *GSS* (encoding the glutathione biosynthesis enzyme glutathione synthetase), *GSR* (encoding glutathione reductase), and *GSTZ1* (encoding the glutathione-dependent enzyme glutathione-S-transferase zeta) (Fig. 4b–d). Numerous other genes encoding a broad range of antioxidant enzymes was upregulated as a consequence of *GLO1* deletion including *CAT* (encoding catalase), *SOD3* (encoding superoxide dismutase 3), and *HMOX1* (encoding heme oxygenase 1). Of note, our oxidative stress gene expression array analysis also revealed that *GLO1*_KO status was associated with significant upregulation of *PTGS1* (encoding the pro-inflammatory enzyme cyclooxygenase-1).

Next, overall cellular oxidative stress was monitored by flow cytometric detection of 2′,7′-dihydrodichlorofluorescein-diacetate (DHDCF) oxidation (Fig. 4e). Remarkably, no changes were observable between *GLO1*_WT and KO cells (not exposed to external electrophilic stressors), even though MG exposure upregulated ROS levels in KO cells to a higher extent than that observable in wildtype cells, an observation documented previously [26]. Consistently, detection of reduced cellular glutathione revealed no changes observable between untreated WT and KO clones, not challenged by exposure to electrophilic stressors (Fig. 4f). Additional evidence in support of a regulatory function of *GLO1* expression in A375 melanoma cell redox homeostasis was derived from the use of a rescue clone generated by CMV-driven *GLO1* re-expression in KO cells (A375-*GLO1*_R), an experimental tool used by us before [26] (supplemental Fig. S2). Our molecular analysis indicated that rescue expression of *GLO1* [associated with restoration of *GLO1* mRNA levels and GLO1 enzymatic activity (supplemental Fig. S2a,b)] reversed *TXNIP* mRNA upregulation (supplemental Fig. S2c). Moreover, rescue expression of *GLO1* reversed MG-induced oxidative stress (supplemental Fig. S2d) and redox-related stress response gene expression (*TXNRD2*, *GSTZ1*, *SRXN1*, *HMOX1*; supplemental Fig. S2e), all of which are associated with *GLO1* deletion in A375 melanoma cells.

Taken together, these data indicate that *GLO1* deletion causes a pronounced alteration of redox regulatory gene expression in A375 melanoma cells characterized by upregulated expression of a broad array of specific redox regulatory factors [including *TXNIP* (Fig. 2a and b), *TXNRD2*, *PRDX2*, *PRDX5*, *SRXN1*, *GSS*, *GSR*, *GSTZ1*, *CAT*, *SOD3*

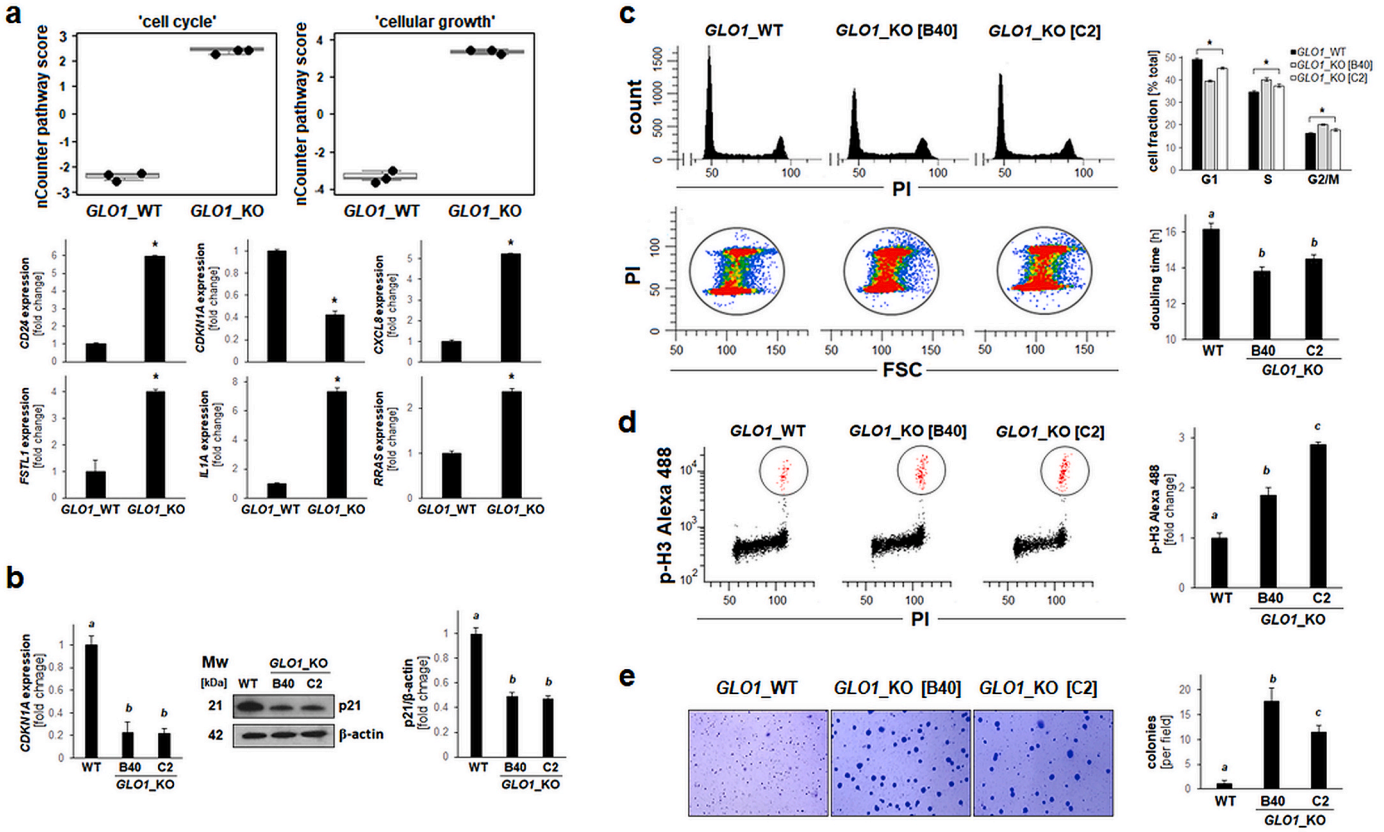

Fig. 5. Genetic deletion of GLO1 shortens population doubling time while increasing M-phase cell cycle population and enhancing clonogenicityof human A375 melanoma cells. (a) NanoString nCounterTM pathway score analysis of 'cell cycle' and 'cellular growth' (top: box plot depiction); single panels (bottom) indicate comparative gene expression [CD24, CDKN1A, CXCL8, FSTL1, IL1A, RRAS]. (b) CDKN1A expression in A375 melanoma (GLO1_WT versus GLO1_KO clones [B40 and C2]) as confirmed by RT-qPCR (left) and immunoblot (right) analysis. Bar graph summarizes protein levels over β-actin control. (c) Alteration of cell cycle and population doubling time: Top panel (left): Representative cell cycle histograms per treatment group as assessed by flow cytometry of PI-stained cells. Top panel (right): Cell cycle distribution as summarized by bar graph depiction. Bottom panel (left): Population shift from G1-towards S- and G2/M-phases as visualized by flow cytometric analysis [PI versus FSC (forward scatter); representative images]. Bottom panel (right): Population doubling time (hr) as determined by proliferation analysis summarized by bar graph depiction. (d) M-phase population assessment as measured by flow cytometry of phospho-histone H3 (Ser10) versus PI-double-stained cells (left panels: representative images); right panel: summary of numerical results as a function of GLO1_KO status. (e) Colony formation was assessed by determining anchorage-independent growth in soft agar; representative images after crystal violet staining (left panels) as summarized by bar graph depiction (right panel). For all bar graph depictions, quantitative data analysis employed ANOVA with Tukey's post hoc test; means without a common letter differ from each other ($p < 0.05$). For bar graphs comparing two groups only, statistical significance was calculated employing the Student's two-tailed *t*-test (*$p < 0.05$). . (For interpretation of the references to colour in this figure legend, the reader is referred to the Web version of this article.)

(Fig. 4)]. These changes might serve compensatory antioxidant functions maintaining redox homeostasis in the absence of *GLO1*.

Genomic *GLO1* deletion shortens population doubling time with increased M-phase cell cycle population and anchorage-independent growth, while limiting A375 melanoma cell invasive potential and metastasis.

Next, guided by NanoString nCounter™ analysis we focused on expression changes consistent with the observed alteration of 'cell cycle regulation' and 'cellular growth' pathway scores observable upon *GLO1* deletion (Fig. 1c and d and 5a). Remarkably, among the most pronounced gene expression changes identified by NanoString™ analysis, many are associated with dysregulated proliferation and cell cycle control during melanomagenesis, including upregulated: *CD24* (9.6-fold), *IL1A* (9.3-fold), *CXCL8* (5.2-fold), *FSTL1* (4.0-fold), *RRAS* (2.4-fold); and downregulated: *CDKN1A* (2.4-fold) [32,51–55]. For example, recent research indicates a crucial role of *CD24* as a cancer stem-like cell marker and driver of anchorage-independent growth and tumorigenesis in cutaneous melanoma [55]. Likewise, upregulation of *CXCL8* and *IL1A* expression has earlier been shown to be involved in increased melanoma cell proliferation, clonogenicity, and tumorigenesis, and an inverse relationship between expression of *IL1A* and *CDKN1A* has been established in a panel of cultured malignant melanoma cells (including A375 cells) [52,53]. Given the importance of *CDKN1A* encoding the cyclin-dependent kinase inhibitor $p21^{Cip1}$, a crucial inhibitor of cell cycle progression, we further confirmed downregulation of *CDKN1A* expression [as already indicated by NanoString™ analysis (Figs. 1b–5a)] by RT-qPCR and immunoblot analysis (Fig. 5b).

Subsequent cell cycle analysis indicated that cells lacking *GLO1* expression displayed a significant increase in S- and G2/M-phase subpopulations (by approximately 5%, each), concomitant with an approximately 10% decrease in the G1-phase subpopulation (Fig. 5c, top panels and bottom, left panels). Further analysis based on flow cytometric detection of the M-phase marker phospho-histone H3 [pH3 (Ser10)] indicated an almost 40% increase in cells transiting through M-phase (out of the total G2/M population) (Fig. 5d). Importantly, phenotypic analysis revealed that A375 cells lacking *GLO1* expression displayed a shortened population doubling time (*GLO1*_WT: 16.17 ± 0.36 h; *GLO1*_KO [B40]: 13.82 ± 0.23 h; *GLO1*_KO [C2]: 14.53 ± 0.24 h;

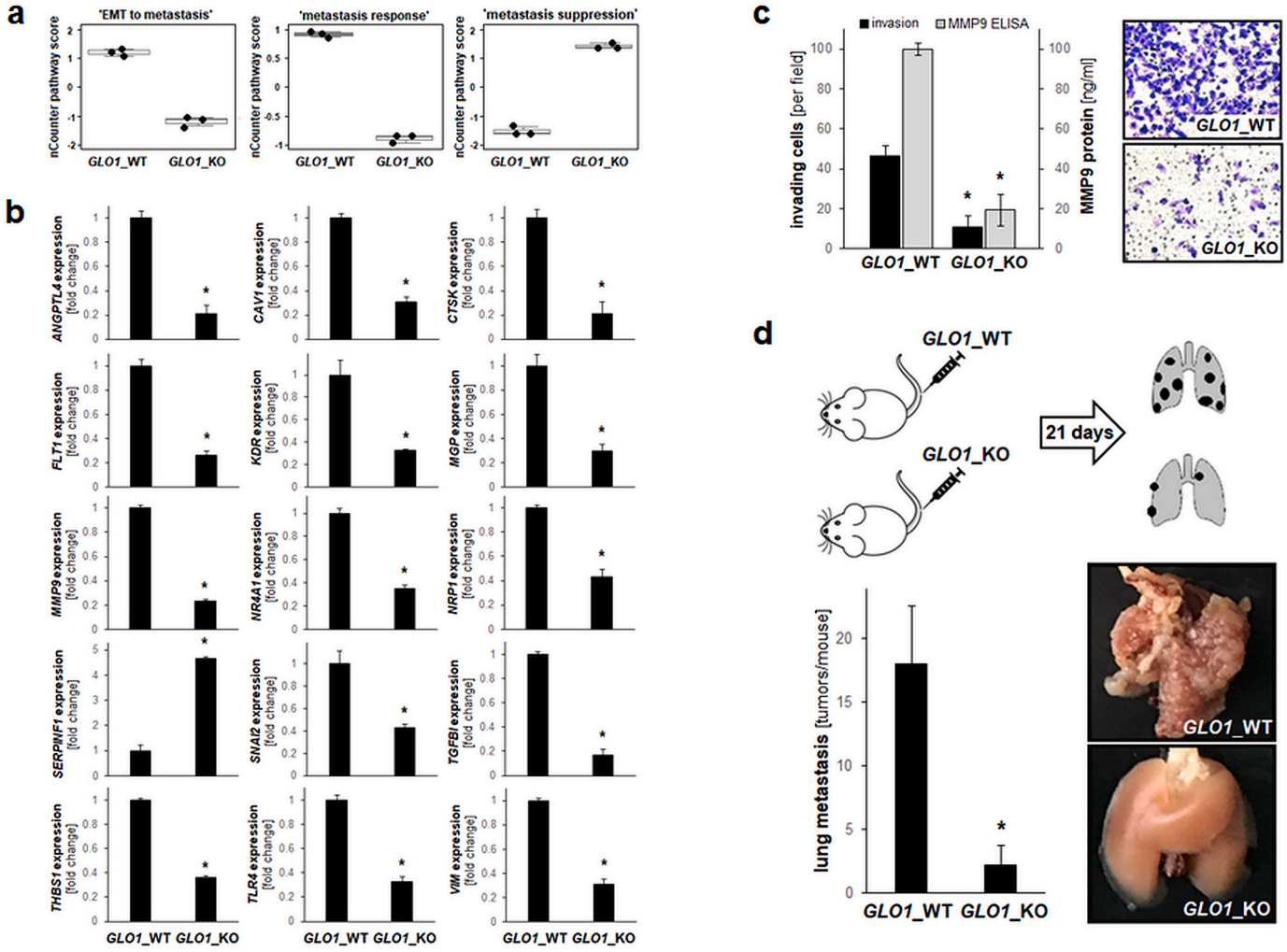

Fig. 6. Genomic *GLO1* deletion antagonizes EMT-related gene expression with suppression of metastasis in a murine melanoma. (a) NanoString nCounter™ pathway score analysis of 'EMT to metastasis', 'metastasis response', and 'metastasis suppression' (box plot depiction). (b) NanoString nCounter™ single gene depiction of EMT- and metastasis-related gene expression. (c) Invasion through Matrigel-coated Boyden chambers (*GLO1*_WT; *GLO1*_KO [B40]); bar graph (left panel) depicts numerical analysis. Left panel also displays MMP9 protein levels in conditioned medium (determined by ELISA analysis); right panel: representative images obtained after crystal violet staining of inserts. (d) Melanoma cells (A375 *GLO1*_WT; *GLO1*_KO [B40]) were tail vein injected (five SCID mice per group) followed by analysis of lung metastasis 21 d later (top panel: experimental scheme). Representative lung specimens are depicted (right panels). Bar graph summarizes numerical analysis of metastases per lung (left panel). For bar graphs comparing two groups only, statistical significance was calculated employing the Student's two-tailed *t*-test (*$p < 0.05$). Nonparametric data analysis of murine experimentation was performed using the Mann–Whitney test (*$p < 0.05$). (For interpretation of the references to colour in this figure legend, the reader is referred to the Web version of this article.)

Fig. 5c, bottom, right panel), a finding consistent with the observed cell cycle alterations, shifting cells towards S- and M-phase (Fig. 5c). In addition, these cells displayed an increased capacity for anchorage-independent growth as confirmed by 3D soft agar colony formation assay documenting an up to 20-fold increase in colony number in *GLO1*_KO clones (Fig. 5e). Taken together, these data indicate that loss of *GLO1* expression is associated with gene expression changes and phenotypic alterations consistent with shortened population doubling time, accelerated cell cycle progression, and increased anchorage-independent growth.

Previously we have identified *GLO1* expression as an important determinant of melanoma cell invasion and metastasis associated with pronounced modulation of epithelial mesenchymal transition (EMT)-related gene expression [26]. NanoString nCounter™ expression profiling largely confirmed and expanded these prior observations (Fig. 6). Specifically, altered expression of gene networks related to '*EMT to metastasis*', '*metastasis response*', and '*metastasis suppression*' were identified by pathway score analysis (Figs. 1c–6a). In addition to expression changes indicative of EMT suppression [as observed before [26]; including downregulation of *MMP9* (5.2-fold), *VIM* (2.7-fold), *and SNAI2* (2.3 fold); Fig. 6b], NanoString™ analysis revealed additional, heretofore unrecognized expression changes [downregulation: *TGFBI* (5.9-fold), *CTSK* (4.7-fold), *ANGPTL4* (4.7-fold), *FLT1* (3.8-fold), *CAV1* (3.2-fold), *MGP* (3.1-fold), *KDR* (3.1-fold), *TLR4* (3.0-fold), *NR4A1* (2.9-fold), *THBS1* (2.8-fold); upregulation: *SERPINF1* (*PEDF*; 4.7-fold); (Fig. 6b)], all with established roles in melanoma invasion and metastasis, and therefore potentially involved in attenuation of EMT in response to *GLO1* deletion [56–63].

Finally, an invasion assay conducted together with ELISA-based determination of extracellular MMP9 levels largely reiterated our published observation that *GLO1*_KO status is associated with significant suppression of melanoma cell invasiveness and MMP9 production (Fig. 6c) [26]. Strikingly, a tail vain injection metastasis model using SCID mice indicated that genetic deletion of *GLO1* significantly attenuates lung metastasis of A375 melanoma cells (Fig. 6d).

Genomic deletion of *GLO1* accelerates tumor growth in a SCID mouse xenograft model of human A375 malignant melanoma.

Next, the impact of genetic *GLO1* status on A375 melanoma tumorigenicity was examined in a relevant SCID mouse model assessing tumor growth after subcutaneous injection (28 d period; Fig. 7a). Strikingly, specific tumor growth rates (% per day) of *GLO1*_KO cell clones significantly surpassed that of wildtype cells (*GLO1*_WT: 9.23; *GLO1*_KO [B40]: 15.24; *GLO1*_KO [C2]: 13.56). Accordingly, average tumor size (mm^3) at the end of the experiment differed greatly as a function of *GLO1* genotype (*GLO1*_WT: 455.8 ± 140.6; *GLO1*_KO [B40]: 1579.2 ± 262.9; *GLO1*_KO [C2]: 1029.7 ± 239.1; Fig. 7a and b).

Next, comparative immunohistochemical analysis of tumor specimens was performed (Fig. 7b and c). First, differential *GLO1* expression status was confirmed at the protein level, and expression of antigens related to proliferation and cell cycle control (p21, Ki67) was consistent with the observed growth rates. Likewise, differential expression of tumor antigens representing metabolic and redox control (TXNIP, SLC2A1, GFPT1) as well as immune evasion (PD-L1) was observed as a function of *GLO1* genotype (Fig. 7c). Concordantly, RT-qPCR analysis of tumor-derived mRNA confirmed critical expression changes [including *CDKN1A*, *TXNIP*, *SLC2A1*, *GFPT1*, *GFPT2*, *MMP9*, *PDL1*] already observed at the cell culture level (Fig. 7d). Taken together, these observations obtained in a murine xenograft model suggest that genomic *GLO1* deletion accelerates tumor growth in a SCID mouse xenograft model of human A375 malignant melanoma.

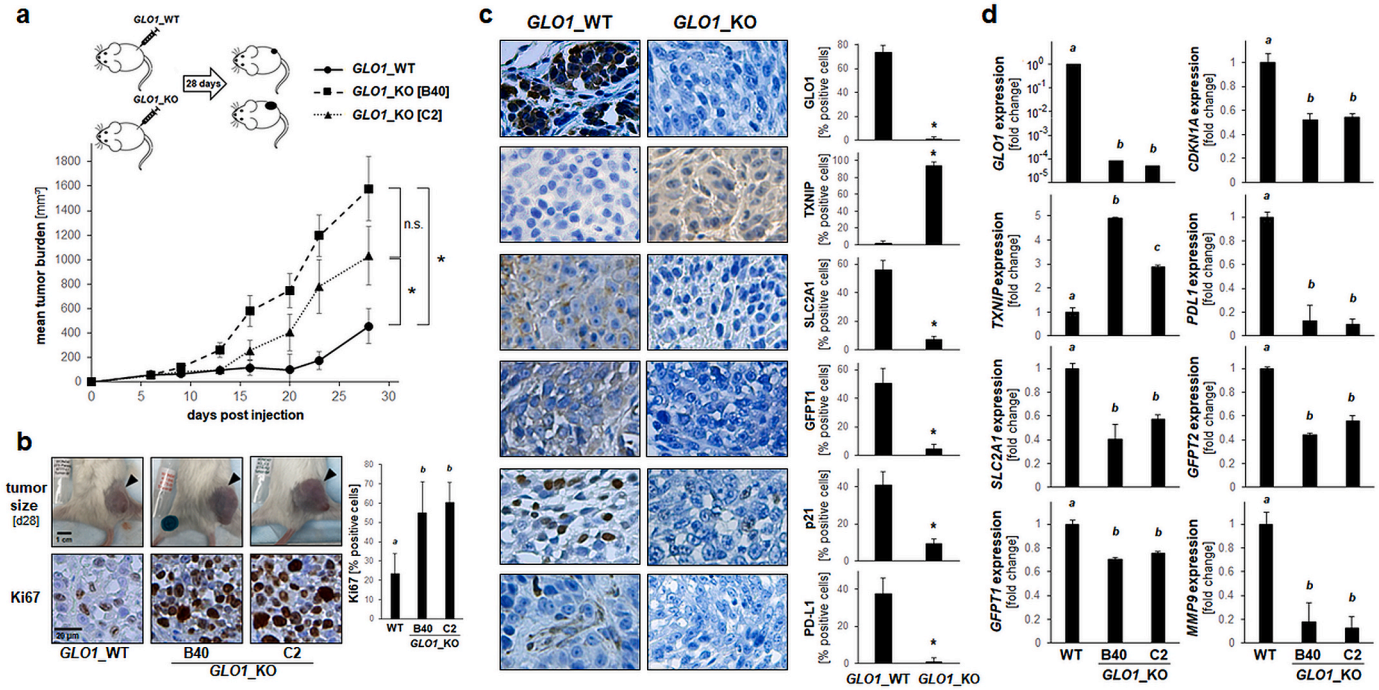

Fig. 7. Genomic *GLO1* deletion accelerates tumor growth in a SCID mouse xenograft model of human A375 malignant melanoma. (a) A375 melanoma cells (three groups: *GLO1*_WT; *GLO1*_KO [B40]; *GLO1*_KO [C2]) were injected subcutaneously (ten mice per group) followed by assessment of tumor growth over a 28 d period; top panel: injection scheme; bottom panel: tumor burden as a function of genotype and time. (b–d) At the end of the experiment, tumors were processed for gene expression analysis by RT-qPCR and immunohistochemical staining. (b) Representative tumor images (dorsal, right flank, s. c.; top panels) with Ki67 immunohistochemical analysis of tumor specimens (bottom panels; 20x magnification) as summarized by bar graph depiction (right panel). (c) Immunohistochemical analysis of tumor specimens (*GLO1*_WT; *GLO1*_KO [B40]; 20x magnification); quantitative analysis as summarized by bar graph depiction (right panels). (d) RT-qPCR assessment of gene expression as a function of tumor *GLO1* genotype (*GLO1*_WT; *GLO1*_KO clones [B40 and C2]). For all bar graph depictions, quantitative data analysis employed ANOVA with Tukey's post hoc test; means without a common letter differ from each other ($p < 0.05$). For bar graphs comparing two groups only, statistical significance was calculated employing the Student's two-tailed *t*-test (*p < 0.05). Nonparametric data analysis of murine experimentation was performed using the Mann–Whitney test (*p < 0.05).

4. Discussion

Cumulative evidence supports a role of *GLO1* expression in tumorigenesis that may involve various mechanisms including alteration of cellular energy and redox homeostasis, defense against electrophilic carbonyl and chemotherapeutic stress, and epigenetic control of histone adduction and gene expression [8,9,11–16]. Specifically, an oncometabolic function of the glycolytic byproduct MG, regulated by the glyoxalase detoxification system, has been substantiated by numerous lines of investigation, and a double-edged, hormetic role of MG, serving pro-proliferative and tumorigenic functions at low concentrations while displaying cytotoxic, anti-proliferative, and tumor-suppressive activities at higher concentrations, has been demonstrated [6,8,11,13,16,24,64].

Here, employing NanoString™-based expression profiling and pathway analysis followed by phenotypic characterization, we have generated novel experimental evidence suggesting that CRISPR/Cas9-based deletion of *GLO1* is accompanied by gene expression changes involved in (*i*) attenuation of melanoma cell glucose uptake and energy metabolism, (*ii*) alteration of redox homeostasis, (*iii*) acceleration of cell cycle progression and proliferation, (*iv*) impairment of invasiveness and metastasis, and (*v*) potentiation of tumor growth in a murine xenograft model.

TXNIP upregulation, the most pronounced gene expression change observed as a consequence of CRISPR/Cas9-based *GLO1* deletion, was a common feature shared between 'cancer metabolism', 'cell cycle', 'proliferative control', and 'EMT to metastasis' pathways as assigned by NanoString™ Pathway Score analysis (Fig. 1). Importantly, a crucial role of the tumor suppressor *TXNIP* and in the control of glucose metabolism, redox homeostasis, and tumorigenic progression has been demonstrated before, attributed largely to thioredoxin antagonism and modulation of thioredoxin-dependent antioxidant enzymes, attenuation of GLUT1-dependent glucose uptake and glycolytic metabolism, HIF1α-antagonism, and miR-dependent antagonistic regulation of EMT-related transcription factors. Binding thioredoxin at the redox-critical site, the tumor suppressor TXNIP antagonizes thioredoxin function, thereby controlling DNA synthesis, transcription factor activity, proliferation (through modulation of peroxiredoxin 1) and apoptosis [through modulation of apoptosis signal-regulating kinase 1 (ASK1)] [41–43,49,50,65–68].

Importantly, in human melanoma, *TXNIP* expression has been shown to inhibit melanoma cell invasiveness without causing an attenuation of proliferative capacity, and B16F10 melanoma cells transfected with *TXNIP* displayed decreased lung metastasis in C57BL/6 mice resulted in decreased, and *TXNIP* has now been identified as a miR-regulated metastasis suppressor predicting melanoma patient survival [65–68].

Given the important role of *TXNIP* as a negative regulator of melanomagenesis, it will be important to elucidate the specific molecular mechanism of *GLO1*-dependent *TXNIP* regulation as supported here for the first time by genetic and pharmacological evidence. In this context, it is tempting to speculate that modulation of cellular MG, now recognized as an important glycolysis-derived oncometabolite involved in various aspects of tumorigenesis, might determine *TXNIP* responsiveness to genomic *GLO1* deletion. Indeed, it will be interesting to examine if control of *TXNIP* expression occurs downstream of the GLO1 metabolite MG, an established electrophilic signaling molecule impacting various molecular targets (including NRF2 and miRs) that are known to regulate *TXNIP* mRNA levels [6,66,69–71]. Our observation that *TXNIP* upregulation occurred in response to GLO1 inhibition by TLSC702 and also in response to treatment with the GLO1 substrate MG supports this hypothesis (Fig. 2f). Moreover, *TXNIP* upregulation was also observable in DU145 prostate carcinoma cells with genomic *GLO1* deletion (Fig. 2d and e). Obviously, more detailed mechanistic studies (performed in a wider range of diverse melanoma cell lines) are required to explore molecular basis and causative role of *GLO1* in the modulation of melanoma cell gene expression (including *TXNIP*) identified by NanoString nCounter™ analysis (Fig. 1).

Remarkably, we were able to demonstrate an attenuation of cellular glucose uptake as a consequence of *GLO1* deletion (Fig. 3b), observable together with downregulation of *SLC2A1* (Figs. 2a and 3f). In contrast, even though cellular ATP levels were not modulated as a function of *GLO1* expression, we observed that OCR was increased in *GLO1*_KO cells with concomitant ECAR reduction as substantiated by Seahorse metabolism analysis, indicative of increased mitochondrial respiration compensating for reduced glucose uptake and glycolytic flux, a hypothesis to be tested by future experiments (Fig. 3c–e). Indeed, alteration of glucose metabolism in *GLO1*_KO cells was evidenced by depletion of key metabolites essential to glycolysis (Glc-6P) and the hexosamine biosynthesis pathway (HBP: GlcN-6P, GlcNAc-6P, UDP-GlcNAc), accompanied by an increase in PPP intermediates (R–5P, Ru–5P) (Fig. 3e). Consistent with a lowering of HBP-related glucose metabolites as result of *GLO1* deletion, we also observed the downregulated expression of hexosamine pacemaker enzymes (encoded by *GFAT1* and *GFAT2*; Fig. 3f and g). Interestingly, HBP inhibition using a small molecule pharmacological GFAT1-inhibitor has recently been identified as a promising cancer drug target blocking metastasis and PD-L1-mediated immune evasion through alteration of extracellular protein glycosylation downstream of UDP-GlcNAc depletion [47]. Future research will aim at elucidating the molecular mechanisms connecting *GLO1* expression status, and modulation of cellular MG metabolism with *TXNIP*-dependent control of glucose metabolism (glycolysis, HBP, PPP), a pathway that might offer novel therapeutic approaches targeting oncometabolism. Indeed, we observed that *PDL1* expression, associated with oncometabolic alterations in various malignancies including malignant melanoma, was suppressed in cultured *GLO1*_KO melanoma cells and tumors (Fig. 3f and g and Fig. 7c and d), opening the possibility that *PDL1* expression, crucial to tumor cell immune evasion, might be amenable to therapeutic modulation by genetic or pharmacological *GLO1* antagonism [48].

Following our key observation of pronounced *TXNIP* upregulation as a result of *GLO1* deletion (Figs. 1 and 2a-c), our subsequent redox-focused gene expression array analysis revealed that upregulated expression of genes controlling glutathione, i.e. biosynthesis (*SLC7A11*, *GSS*), regeneration (*GSR*), and glutathione-dependent detoxification (*GPX1*, *GPX4*, *GSTZ1*, *GSTP1*) (Fig. 4a–d). Moreover, as a consequence of *GLO1* deletion, alteration of the thioredoxin-related antioxidant network (*TXN*, *TXNRD1*, *TXNRD2*, *PRDX1*, *PRDX2*, *PRDX3*, *PRDX5*, *SRXN1*) together with upregulated expression of other major antioxidant defense factors including catalase (*CAT*) and extracellular superoxide dismutase 3 (*SOD3*) were observed. These pronounced expression changes [together with detection of elevated levels of PPP intermediates (Fig. 3a)] might be indicative of an adaptational change in redox homeostasis as a result of *GLO1* deletion and *TXNIP* upregulation, consistent with the observation that no significant alteration of baseline cellular oxidative stress and glutathione levels were detectable in cells unless challenged by external MG (Fig. 4e and f). Further evidence in support of *GLO1* control of *TXNIP* and redox response gene expression was obtained from the observation that rescue expression of *GLO1* reversed *TXNIP* upregulation, redox-related stress response gene expression (*TXNRD2*, *GSTZ1*, *SRXN1*, *HMOX1*), and MG-induced oxidative stress, all of which are associated with *GLO1* deletion in A375 melanoma cells (supplemental Fig. S2).

Guided by NanoString™ pathway score analysis, we also focused on the phenotypic assessment of proliferation, cell cycle progression, and clonogenicity as a function of *GLO1*_KO status (Fig. 5). Indeed, our cell cycle and proliferation analysis indicated an increase in cell populations in S- and M-phase, a decrease in population doubling time, and an increase in anchorage-independent growth/clonogenicity. These phenotypic characteristics are consistent with gene expression changes observable in *GLO1*_KO cells (including *CD24*, *CXCL8*, *IL1A*), all of which have been shown before to upregulate melanoma cell proliferative capacity, anchorage-independent growth, and tumorigenicity [32,52,53,55]. Likewise, NanoString™ pathway score analysis indicated

downregulation of *CDKN1A* [encoding p21 (CIP1/WAF1), the cyclin dependent kinase inhibitor and suppressor of cell cycle progression], confirmed by us independently by RT-qPCR and immunoblot analysis.

NanoString™ analysis also revealed significant modulation of EMT-related genes that occurs in response to *GLO1*_KO status, confirming and expanding our prior data that have already identified expression changes of numerous EMT-related genes (including *MMP9*, *SNAI2, VIM*) observable in *GLO1*_KO A375 melanoma cells (Fig. 6) [26]. Strikingly, a large number of genes shown here for the first time to be responsive to *GLO1* expression status (including *TXNIP*, *ANGPTL4*, *CAV1*, *CTSK*, *FLT1*, *KDR*, *NRP1*, *NR4A1*, *SERPINF1*, *TGFBI*, *THSB1*, *TLR4*) have previously been associated with EMT in melanomagenesis [56–63,65]. For example, concerted upregulation of VEGF-receptor expression (*FLT1*, *KDR*, *NRP1*) together with trombospondin-1 (*THSB1*) has been associated with melanoma progression [56]. Likewise, *TLR4* has been identified as a driver of melanoma metastasis and angiotropism, and *SERPINF1* (upregulated in response to *GLO1*_KO status) encoding pigment epithelium-derived factor (PEDF) is an established anti-metastatic and anti-angiogenic factor in human melanoma [59,61,72]. As observed before, invasive potential of A375 melanoma cells was downregulated *in vitro* (Fig. 6c), and metastasis was suppressed *in vivo* as a consequence of *GLO1*_KO status (Fig. 6d)] [26].

In striking contrast to impaired metastatic potential and consistent with increased proliferative capacity and cell cycle alterations observed *in vitro* (Fig. 5), tumor growth rate of *GLO1*_KO as compared to wildtype cells was accelerated significantly (Fig. 7). Interestingly, immunohistochemical analysis confirmed the sustained maintenance of key expression changes associated with *GLO1*_KO status (upregulated: *TXNIP;* downregulated*: GLUT1, GFAT1*, GFAT2, *CDKN1A*) together with upregulation of the proliferation marker Ki-67. Also, tumor *MMP9* expression was downregulated, an observation consistent with inhibition of EMT and metastatic potential, as documented and discussed before [22, 26]. Strikingly, as already observed in cell culture (Fig. 3f and g), downregulation of *PDL1* expression was maintained in tumors lacking *GLO1* expression, an observation confirmed at the mRNA and protein levels (Fig. 7c and d).

Taken together, these data indicate that *GLO1* deletion from A375 melanoma cells is associated with pronounced acceleration of *in vivo* tumorigenicity that, paradoxically, occurs with attenuation of metastatic potential. This striking phenotype is consistent with our NanoString nCounter™ gene expression profiling revealing alterations that impact energy metabolism, redox homeostasis, proliferative and cell cycle control, and EMT/metastatic potential. Interestingly, the development of metastatic melanoma has been shown to require the dynamic shift of malignant cells between proliferative and invasive phenotypes, and it is therefore possible that decreased metastatic potential downstream of *GLO1* elimination is associated with increased proliferative capacity as observed by us (Figs. 5–7) [73–75]. Specifically, cumulative evidence suggests that melanoma aggressiveness originates from an intrinsic plasticity referred to as 'phenotype switching' driving tumor progression, allowing the dynamic, reversible, and seemingly paradoxical transformation of malignant cells between a hyper-proliferative/hypo-invasive to a hypo-proliferative/hyper-invasive stage [73–75]. Thus, it might be hypothesized that this molecular switch is amenable to modulation by *GLO1* elimination or pharmacological intervention as observed here for the first time. In this context, it also seems worth mentioning that our *in vivo* experiments were conducted in immunosuppressed SCID mice, producing seemingly opposing tumor-relevant outcomes, i.e. (*i*) attenuated lung metastasis and (*ii*) accelerated tumor growth (Figs. 6 and 7, respectively). Thus, in order to reconcile these findings and to define the potential therapeutic value of *GLO1* antagonism, our ongoing experiments aim at examining the possibility that GLO1-inhibition (potentially associated with enhanced tumorigenic potential) might be counterbalanced by increased tumor immunogenicity (downstream of downregulated *PDL1* expression) and attenuation of metastasis in immunocompetent host systems.

Future research has to elucidate the specific molecular basis underlying *GLO1* control of melanoma cell tumorigenicity and invasiveness observed here in A375 cells, using a more comprehensive panel of melanoma cells representative of the human disease and elucidating the mechanistic involvement of novel targets shown here for the first time to be responsive to genetic *GLO1* modulation (including *TXNIP*, *GFAT1*, and *PDL1*). Importantly, given the documented efficacy of small molecule pharmacological inhibitors, our observations suggest feasibility of therapeutic intervention targeting *GLO1* control of glucose utilization, redox homeostasis, cell proliferation, metastasis, and immune evasion, a hypothesis to be explored by future experimentation.

Declaration of competing interest

All authors declare that there are no conflicts of interest to disclose.

Acknowledgements

Supported in part by grants from the National Institutes of Health (1R01CA229418, 1R03CA230949, 1R21ES029579, 1P01CA229112, ES007091, ES006694, and UA Cancer Center Support Grant CA023074). The content is solely the responsibility of the authors and does not necessarily represent the official views of the National Cancer Institute or the National Institutes of Health.

Appendix A. Supplementary data

Supplementary data to this article can be found online at https://doi.org/10.1016/j.redox.2020.101838.

References

[1] J. Paluncic, Z. Kovacevic, P.J. Jansson, D. Kalinowski, A.M. Merlot, M.L. Huang, H. C. Lok, S. Sahni, D.J. Lane, D.R. Richardson, Roads to melanoma: key pathways and emerging players in melanoma progression and oncogenic signaling, Biochim. Biophys. Acta 1863 (2016) 770–784.

[2] J.J. Luke, K.T. Flaherty, A. Ribas, G.V. Long, Targeted agents and immunotherapies: optimizing outcomes in melanoma, Nat. Rev. Clin. Oncol. 14 (2017) 463–482.

[3] H. Helgadottir, I. Rocha Trocoli Drakensjo, A. Girnita, Personalized medicine in malignant melanoma: towards patient tailored treatment, Front Oncol 8 (2018) 202.

[4] G. Cesi, G. Walbrecq, A. Zimmer, S. Kreis, C. Haan, ROS production induced by BRAF inhibitor treatment rewires metabolic processes affecting cell growth of melanoma cells, Mol. Canc. 16 (2017) 102.

[5] B.I. Ratnikov, D.A. Scott, A.L. Osterman, J.W. Smith, Z.A. Ronai, Metabolic rewiring in melanoma, Oncogene 36 (2017) 147–157.

[6] M.J. Bollong, G. Lee, J.S. Coukos, H. Yun, C. Zambaldo, J.W. Chang, E.N. Chin, I. Ahmad, A.K. Chatterjee, L.L. Lairson, P.G. Schultz, R.E. Moellering, A metabolite-derived protein modification integrates glycolysis with KEAP1-NRF2 signalling, Nature 562 (2018) 600–604.

[7] N. Rabbani, M. Xue, M.O. Weickert, P.J. Thornalley, Multiple roles of glyoxalase 1-mediated suppression of methylglyoxal glycation in cancer biology-Involvement in tumour suppression, tumour growth, multidrug resistance and target for chemotherapy, Semin. Canc. Biol. 49 (2018) 83–93.

[8] M.J. Nokin, F. Durieux, J. Bellier, O. Peulen, K. Uchida, D.A. Spiegel, J. R. Cochrane, C.A. Hutton, V. Castronovo, A. Bellahcene, Hormetic potential of methylglyoxal, a side-product of glycolysis, in switching tumours from growth to death, Sci. Rep. 7 (2017) 11722.

[9] N. Shimada, R. Takasawa, S.I. Tanuma, Interdependence of GLO I and PKM2 in the Metabolic shift to escape apoptosis in GLO I-dependent cancer cells, Arch. Biochem. Biophys. 638 (2018) 1–7.

[10] A. Hutschenreuther, M. Bigl, N.Y. Hemdan, T. Debebe, F. Gaunitz, G. Birkenmeier, Modulation of GLO1 expression affects malignant properties of cells, Int. J. Mol. Sci. 17 (2016) 2133.

[11] C. Antognelli, L. Mezzasoma, K. Fettucciari, V.N. Talesa, A novel mechanism of methylglyoxal cytotoxicity in prostate cancer cells, Int. J. Biochem. Cell Biol. 45 (2013) 836–844.

[12] M.J. Nokin, F. Durieux, P. Peixoto, B. Chiavarina, O. Peulen, A. Blomme, A. Turtoi, B. Costanza, N. Smargiasso, D. Baiwir, J.L. Scheijen, C.G. Schalkwijk, J. Leenders, P. De Tullio, E. Bianchi, M. Thiry, K. Uchida, D.A. Spiegel, J.R. Cochrane, C. A. Hutton, E. De Pauw, P. Delvenne, D. Belpomme, V. Castronovo, A. Bellahcene, Methylglyoxal, a glycolysis side-product, induces Hsp90 glycation and YAP-mediated tumor growth and metastasis, Elife 5 (2016) 19375.

[13] M.J. Nokin, J. Bellier, F. Durieux, O. Peulen, G. Rademaker, M. Gabriel, C. Monseur, B. Charloteaux, L. Verbeke, S. van Laere, P. Roncarati, M. Herfs,

C. Lambert, J. Scheijen, C. Schalkwijk, A. Colige, J. Caers, P. Delvenne, A. Turtoi, V. Castronovo, A. Bellahcene, Methylglyoxal, a glycolysis metabolite, triggers metastasis through MEK/ERK/SMAD1 pathway activation in breast cancer, Breast Cancer Res. 21 (2019) 11.
[14] Q. Zheng, N.D. Omans, R. Leicher, A. Osunsade, A.S. Agustinus, E. Finkin-Groner, H. D'Ambrosio, B. Liu, S. Chandarlapaty, S. Liu, Y. David, Reversible histone glycation is associated with disease-related changes in chromatin architecture, Nat. Commun. 10 (2019) 1289.
[15] Q. Zheng, A. Osunsade, Y. David, Protein arginine deiminase 4 antagonizes methylglyoxal-induced histone glycation, Nat. Commun. 11 (2020) 3241.
[16] B. Chiavarina, M.J. Nokin, J. Bellier, F. Durieux, N. Bletard, F. Sherer, P. Lovinfosse, O. Peulen, L. Verset, R. Dehon, P. Demetter, A. Turtoi, K. Uchida, S. Goldman, R. Hustinx, P. Delvenne, V. Castronovo, A. Bellahcene, Methylglyoxal-mediated stress correlates with high metabolic activity and promotes tumor growth in colorectal cancer, Int. J. Mol. Sci. 18 (2017) 213.
[17] P.J. Thornalley, L.G. Edwards, Y. Kang, C. Wyatt, N. Davies, M.J. Ladan, J. Double, Antitumour activity of S-p-bromobenzylglutathione cyclopentyl diester in vitro and in vivo. Inhibition of glyoxalase I and induction of apoptosis, Biochem. Pharmacol. 51 (1996) 1365–1372.
[18] T. Santarius, G.R. Bignell, C.D. Greenman, S. Widaa, L. Chen, C.L. Mahoney, A. Butler, S. Edkins, S. Waris, P.J. Thornalley, P.A. Futreal, M.R. Stratton, GLO1-A novel amplified gene in human cancer, Genes Chromosomes Cancer 49 (2010) 711–725.
[19] H. Taniguchi, M. Horinaka, T. Yoshida, K. Yano, A.E. Goda, S. Yasuda, M. Wakada, T. Sakai, Targeting the glyoxalase pathway enhances TRAIL efficacy in cancer cells by downregulating the expression of antiapoptotic molecules, Mol. Canc. Therapeut. 11 (2012) 2294–2300.
[20] S. Zhang, X. Liang, X. Zheng, H. Huang, X. Chen, K. Wu, B. Wang, S. Ma, Glo1 genetic amplification as a potential therapeutic target in hepatocellular carcinoma, Int. J. Clin. Exp. Pathol. 7 (2014) 2079–2090.
[21] R. Takasawa, N. Shimada, H. Uchiro, S. Takahashi, A. Yoshimori, S. Tanuma, TLSC702, a novel inhibitor of human glyoxalase I, induces apoptosis in tumor cells, Biol. Pharm. Bull. 39 (2016) 869–873.
[22] C. Antognelli, R. Cecchetti, F. Riuzzi, M.J. Peirce, V.N. Talesa, Glyoxalase 1 sustains the metastatic phenotype of prostate cancer cells via EMT control, J. Cell Mol. Med. 22 (2018) 2865–2883.
[23] N.A. Al-Shar'i, Q.A. Al-Balas, R.A. Al-Waqfi, M.A. Hassan, A.E. Alkhalifa, N. M. Ayoub, Discovery of a nanomolar inhibitor of the human glyoxalase-I enzyme using structure-based poly-pharmacophore modelling and molecular docking, J. Comput. Aided Mol. Des. 33 (2019) 799–815.
[24] C. Antognelli, S. Moretti, R. Frosini, E. Puxeddu, A. Sidoni, V.N. Talesa, Methylglyoxal acts as a tumor-promoting factor in anaplastic thyroid cancer, Cells 8 (2019) 547.
[25] W.B. Bair 3rd, C.M. Cabello, K. Uchida, A.S. Bause, G.T. Wondrak, GLO1 overexpression in human malignant melanoma, Melanoma Res. 20 (2010) 85–96.
[26] J. Jandova, J. Perer, A. Hua, J.A. Snell, G.T. Wondrak, Genetic target modulation employing CRISPR/Cas9 identifies glyoxalase 1 as a novel molecular determinant of invasion and metastasis in A375 human malignant melanoma cells in vitro and in vivo, Cancers 12 (2020) 1369.
[27] G.K. Geiss, R.E. Bumgarner, B. Birditt, T. Dahl, N. Dowidar, D.L. Dunaway, H. P. Fell, S. Ferree, R.D. George, T. Grogan, J.J. James, M. Maysuria, J.D. Mitton, P. Oliveri, J.L. Osborn, T. Peng, A.L. Ratcliffe, P.J. Webster, E.H. Davidson, L. Hood, Direct multiplexed measurement of gene expression with color-coded probe pairs, Nat. Biotechnol. 26 (2008) 317–325.
[28] M.M. Kulkarni, Digital multiplexed gene expression analysis using the NanoString nCounter system, Curr Protoc Mol Biol (2011) 25B.10.1–25B.10.17. https://pubmed.ncbi.nlm.nih.gov/21472696/.
[29] M. Long, S. Tao, M. Rojo de la Vega, T. Jiang, Q. Wen, S.L. Park, D.D. Zhang, G. T. Wondrak, Nrf2-dependent suppression of colon carcinogenesis by the cinnamon-derived dietary factor cinnamaldehyde, Canc. Prev. Res. 8 (2015) 444–454.
[30] A.L. Davis, S. Qiao, J.L. Lesson, M. Rojo de la Vega, S.L. Park, C.M. Seanez, V. Gokhale, C.M. Cabello, G.T. Wondrak, The quinone methide aurin is a heat shock response inducer that causes proteotoxic stress and Noxa-dependent apoptosis in malignant melanoma cells, J. Biol. Chem. 290 (2015) 1623–1638.
[31] J. Perer, J. Jandova, J. Fimbres, E.Q. Jennings, J.J. Galligan, A. Hua, G. T. Wondrak, The sunless tanning agent dihydroxyacetone induces stress response gene expression and signaling in cultured human keratinocytes and reconstructed epidermis, Redox Biology 36 (2020) 101594.
[32] C.M. Cabello, W.B. Bair, S. Ley, S.D. Lamore, S. Azimian, G.T. Wondrak, The experimental chemotherapeutic N-6-furfuryladenosine (kinetin-riboside) induces rapid ATP depletion, genotoxic stress, and CDKN1A (p21) upregulation in human cancer cell lines, Biochem. Pharmacol. 77 (2009) 1125–1138.
[33] J. Han, S. Gagnon, T. Eckle, C.H. Borchers, Metabolomic analysis of key central carbon metabolism carboxylic acids as their 3-nitrophenylhydrazones by UPLC/ESI-MS, Electrophoresis 34 (2013) 2891–2900.
[34] J. Han, V. Tschernutter, J. Yang, T. Eckle, C.H. Borchers, Analysis of selected sugars and sugar phosphates in mouse heart tissue by reductive amination and liquid chromatography-electrospray ionization mass spectrometry, Anal. Chem. 85 (2013) 5965–5973.
[35] C.H. Zou, Y.J. Wang, Z.F. Shen, 2-NBDG as a fluorescent indicator for direct glucose uptake measurement, J. Biochem. Biophys. Methods 64 (2005) 207–215.
[36] J. Janda, V. Nfonsam, F. Calienes, J.E. Sligh, J. Jandova, Modulation of ROS levels in fibroblasts by altering mitochondria regulates the process of wound healing, Arch. Dermatol. Res. 308 (2016) 239–248.
[37] C.M. Cabello, S.D. Lamore, W.B. Bair 3rd, S. Qiao, S. Azimian, J.L. Lesson, G. T. Wondrak, The redox antimalarial dihydroartemisinin targets human metastatic melanoma cells but not primary melanocytes with induction of NOXA-dependent apoptosis, Invest. N. Drugs 30 (2012) 1289–1301.
[38] J. Jandova, C.J. Mason, S.C. Pawar, G.S. Watts, Fn14 receptor promotes invasive potential and metastatic capacity of non-small lung adenocarcinoma cells through the up-regulation of integrin alpha6, Neoplasma 62 (2015) 41–52.
[39] E. Mehrara, E. Forssell-Aronsson, H. Ahlman, P. Bernhardt, Specific growth rate versus doubling time for quantitative characterization of tumor growth rate, Cancer Res 67 (2007) 3970–3975.
[40] R. Takasawa, A. Tao, K. Saeki, N. Shionozaki, R. Tanaka, H. Uchiro, S. Takahashi, A. Yoshimori, S. Tanuma, Discovery of a new type inhibitor of human glyoxalase I by myricetin-based 4-point pharmacophore, Bioorg. Med. Chem. Lett 21 (2011) 4337–4342.
[41] N.M. Alhawiti, S. Al Mahri, M.A. Aziz, S.S. Malik, S. Mohammad, TXNIP in metabolic regulation: physiological role and therapeutic outlook, Curr. Drug Targets 18 (2017) 1095–1103.
[42] B.R. Wilde, D.E. Ayer, Interactions between Myc and MondoA transcription factors in metabolism and tumourigenesis, Br. J. Canc. 113 (2015) 1529–1533.
[43] N. Wu, B. Zheng, A. Shaywitz, Y. Dagon, C. Tower, G. Bellinger, C.H. Shen, J. Wen, J. Asara, T.E. McGraw, B.B. Kahn, L.C. Cantley, AMPK-dependent degradation of TXNIP upon energy stress leads to enhanced glucose uptake via GLUT1, Mol Cell 49 (2013) 1167–1175.
[44] V. Audrito, S. Serra, A. Stingi, F. Orso, F. Gaudino, C. Bologna, F. Neri, G. Garaffo, R. Nassini, G. Baroni, E. Rulli, D. Massi, S. Oliviero, R. Piva, D. Taverna, M. Mandala, S. Deaglio, PD-L1 up-regulation in melanoma increases disease aggressiveness and is mediated through miR-17-5p, Oncotarget 8 (2017) 15894–15911.
[45] S. Kouidhi, F. Ben Ayed, A. Benammar Elgaaied, Targeting tumor metabolism: a new challenge to improve immunotherapy, Front. Immunol. 9 (2018) 353.
[46] Z. Jiang, Z. Liu, M. Li, C. Chen, X. Wang, Increased glycolysis correlates with elevated immune activity in tumor immune microenvironment, EBioMedicine 42 (2019) 431–442.
[47] N.S. Sharma, V.K. Gupta, V.T. Garrido, R. Hadad, B.C. Durden, K. Kesh, B. Giri, A. Ferrantella, V. Dudeja, A. Saluja, S. Banerjee, Targeting tumor-intrinsic hexosamine biosynthesis sensitizes pancreatic cancer to anti-PD1 therapy, J. Clin. Invest. 130 (2020) 451–465.
[48] V. Petrova, I. Arkhypov, R. Weber, C. Groth, P. Altevogt, J. Utikal, V. Umansky, Modern aspects of immunotherapy with checkpoint inhibitors in melanoma, Int. J. Mol. Sci. 21 (2020) E2367, pii.
[49] O.N. Spindel, C. World, B.C. Berk, Thioredoxin interacting protein: redox dependent and independent regulatory mechanisms, Antioxidants Redox Signal. 16 (2012) 587–596.
[50] E. Yoshihara, S. Masaki, Y. Matsuo, Z. Chen, H. Tian, J. Yodoi, Thioredoxin/Txnip: redoxisome, as a redox switch for the pathogenesis of diseases, Front. Immunol. 4 (2014) 514.
[51] C. Stove, F. Vanrobaeys, B. Devreese, J. Van Beeumen, M. Mareel, M. Bracke, Melanoma cells secrete follistatin, an antagonist of activin-mediated growth inhibition, Oncogene 23 (2004) 5330–5339.
[52] Y. Qin, S. Ekmekcioglu, P. Liu, L.M. Duncan, G. Lizee, N. Poindexter, E.A. Grimm, Constitutive aberrant endogenous interleukin-1 facilitates inflammation and growth in human melanoma, Mol. Canc. Res. 9 (2011) 1537–1550.
[53] S. Wu, S. Singh, M.L. Varney, S. Kindle, R.K. Singh, Modulation of CXCL-8 expression in human melanoma cells regulates tumor growth, angiogenesis, invasion, and metastasis, Cancer Med 1 (2012) 306–317.
[54] H. Sung, K.L. Kanchi, X. Wang, K.S. Hill, J.L. Messina, J.H. Lee, Y. Kim, N.D. Dees, L. Ding, J.K. Teer, S. Yang, A.A. Sarnaik, V.K. Sondak, J.J. Mule, R.K. Wilson, J. S. Weber, M. Kim, Inactivation of RASA1 promotes melanoma tumorigenesis via R-Ras activation, Oncotarget 7 (2016) 23885–23896.
[55] M.R. Tang, J.Y. Guo, D. Wang, N. Xu, Identification of CD24 as a marker for tumorigenesis of melanoma, OncoTargets Ther. 11 (2018) 3401–3406.
[56] O. Straume, L.A. Akslen, Increased expression of VEGF-receptors (FLT-1, KDR, NRP-1) and thrombospondin-1 is associated with glomeruloid microvascular proliferation, an aggressive angiogenic phenotype, in malignant melanoma, Angiogenesis 6 (2003) 295–301.
[57] M.J. Quintanilla-Dieck, K. Codriansky, M. Keady, J. Bhawan, T.M. Runger, Cathepsin K in melanoma invasion, J. Invest. Dermatol. 128 (2008) 2281–2288.
[58] A.G. Smith, W. Lim, M. Pearen, G.E.O. Muscat, R.A. Sturm, Regulation of NR4A nuclear receptor expression by oncogenic BRAF in melanoma cells, Pigment Cell Melanoma Res 24 (2011) 551–563.
[59] S.P. Becerra, V. Notario, The effects of PEDF on cancer biology: mechanisms of action and therapeutic potential, Nat. Rev. Canc. 13 (2013) 258–271.
[60] L. Lauden, J. Siewiera, W. Boukouaci, K. Ramgolam, S. Mourah, C. Lebbe, D. Charron, F. Aoudjit, N. Jabrane-Ferrat, R. Al-Daccak, TGF-beta-induced (TGFBI) protein in melanoma: a signature of high metastatic potential, J. Invest. Dermatol. 134 (2014) 1675–1685.
[61] T. Bald, T. Quast, J. Landsberg, M. Rogava, N. Glodde, D. Lopez-Ramos, J. Kohlmeyer, S. Riesenberg, D. van den Boorn-Konijnenberg, C. Homig-Holzel, R. Reuten, B. Schadow, H. Weighardt, D. Wenzel, I. Helfrich, D. Schadendorf, W. Bloch, M.E. Bianchi, C. Lugassy, R.L. Barnhill, M. Koch, B.K. Fleischmann, I. Forster, W. Kastenmuller, W. Kolanus, M. Holzel, E. Gaffal, T. Tuting, Ultraviolet-radiation-induced inflammation promotes angiotropism and metastasis in melanoma, Nature 507 (2014) 109–113.
[62] I.L. Popa, A.L. Milac, L.E. Sima, P.R. Alexandru, F. Pastrama, C.V. Munteanu, G. Negroiu, Cross-talk between dopachrome tautomerase and caveolin-1 is melanoma cell phenotype-specific and potentially involved in tumor progression, J. Biol. Chem. 291 (2016) 12481–12500.

[63] S. Izraely, S. Ben-Menachem, O. Sagi-Assif, T. Meshel, D.M. Marzese, S. Ohe, I. Zubrilov, M. Pasmanik-Chor, D.S.B. Hoon, I.P. Witz, ANGPTL4 promotes the progression of cutaneous melanoma to brain metastasis, Oncotarget 8 (2017) 75778–75796.
[64] S. Tamori, Y. Nozaki, H. Motomura, H. Nakane, R. Katayama, C. Onaga, E. Kikuchi, N. Shimada, Y. Suzuki, M. Noike, Y. Hara, K. Sato, T. Sato, K. Yamamoto, T. Hanawa, M. Imai, R. Abe, A. Yoshimori, R. Takasawa, S.I. Tanuma, K. Akimoto, Glyoxalase 1 gene is highly expressed in basal-like human breast cancers and contributes to survival of ALDH1-positive breast cancer stem cells, Oncotarget 9 (2018) 36515–36529.
[65] S.F. Goldberg, M.E. Miele, N. Hatta, M. Takata, C. Paquette-Straub, L.P. Freedman, D.R. Welch, Melanoma metastasis suppression by chromosome 6: evidence for a pathway regulated by CRSP3 and TXNIP, Cancer Res 63 (2003) 432–440.
[66] S. Knoll, K. Furst, B. Kowtharapu, U. Schmitz, S. Marquardt, O. Wolkenhauer, H. Martin, B.M. Putzer, E2F1 induces miR-224/452 expression to drive EMT through TXNIP downregulation, EMBO Rep. 15 (2014) 1315–1329.
[67] K. Li, M. Tang, S. Tong, C. Wang, Q. Sun, M. Lv, X. Sun, T. Wang, S. Jin, BRAFi induced demethylation of miR-152-5p regulates phenotype switching by targeting TXNIP in cutaneous melanoma, Apoptosis 25 (2020) 179–191.
[68] D. Shin, J.H. Jeon, M. Jeong, H.W. Suh, S. Kim, H.C. Kim, O.S. Moon, Y.S. Kim, J. W. Chung, S.R. Yoon, W.H. Kim, I. Choi, VDUP1 mediates nuclear export of HIF1alpha via CRM1-dependent pathway, Biochim. Biophys. Acta 1783 (2008) 838–848.
[69] X. He, Q. Ma, Redox regulation by nuclear factor erythroid 2-related factor 2: gatekeeping for the basal and diabetes-induced expression of thioredoxin-interacting protein, Mol. Pharmacol. 82 (2012) 887–897.
[70] H. Liu, N. Zhang, D. Tian, MiR-30b is involved in methylglyoxal-induced epithelial-mesenchymal transition of peritoneal mesothelial cells in rats, Cell. Mol. Biol. Lett. 19 (2014) 315–329.
[71] V.R. Sanghvi, J. Leibold, M. Mina, P. Mohan, M. Berishaj, Z. Li, M.M. Miele, N. Lailler, C. Zhao, E. de Stanchina, A. Viale, L. Akkari, S.W. Lowe, G. Ciriello, R. C. Hendrickson, H.G. Wendel, The oncogenic action of NRF2 depends on de-glycation by fructosamine-3-kinase, Cell 178 (2019) 807–819, e821.
[72] S.E. Dickinson, G.T. Wondrak, TLR4 in skin cancer: from molecular mechanisms to clinical interventions, Mol. Carcinog. 58 (2019) 1086–1093.
[73] K.S. Hoek, O.M. Eichhoff, N.C. Schlegel, U. Dobbeling, N. Kobert, L. Schaerer, S. Hemmi, R. Dummer, In vivo switching of human melanoma cells between proliferative and invasive states, Cancer Res 68 (2008) 650–656.
[74] K.S. Hoek, C.R. Goding, Cancer stem cells versus phenotype-switching in melanoma, Pigment Cell Melanoma Res 23 (2010) 746–759.
[75] E. Tuncer, R.R. Calcada, D. Zingg, S. Varum, P. Cheng, S.N. Freiberger, C.X. Deng, I. Kleiter, M.P. Levesque, R. Dummer, L. Sommer, SMAD signaling promotes melanoma metastasis independently of phenotype switching, J. Clin. Invest. 129 (2019) 2702–2716.